An adaptive cabin air recirculation strategy for an electric truck using a coupled CFD-thermoregulation approach

International Journal of Heat and Mass Transfer 221 (2024) 125056

Contents lists available at ScienceDirect

International Journal of Heat and Mass Transfer

journal homepage: www.elsevier.com/locate/ijhmt

An adaptive cabin air recirculation strategy for an electric truck using a coupled CFD-thermoregulation approach ☆

Anandh Ramesh Babu [a,*], Simone Sebben [a], Zenitha Chronéer [b], Sassan Etemad [a,b]

[a] Chalmers University of Technology, Gothenburg, Sweden
[b] Volvo Group Truck Technology, Gothenburg, Sweden

ARTICLE INFO

Keywords:
Return air strategy
Low-temperature cabin climatization
CFD-thermoregulation co-simulation
Cabin thermal comfort
Electric vehicles

ABSTRACT

Cabin climatization is one of the largest auxiliary loads in an electric vehicle, and its performance significantly affects the driving range. Recirculating climatized air from the cabin has been shown to reduce energy consumption, but at the risk of fogging the windows and deteriorating the air quality. Therefore, many automobile manufacturers refrain from adopting it at low ambient temperatures. In this paper, an adaptive recirculation strategy that takes these issues into account is proposed and studied on an electric truck cabin while heating. Numerical simulations were performed using a coupled CFD-thermoregulation model, with the consideration of humidity and CO_2. The JOS-3 thermoregulation model was employed for estimations of skin temperatures and evaporation of vapor from the skin, and the Berkeley comfort model was used to evaluate the comfort metrics. Ten scenarios were considered at various vehicle speeds, temperatures, and relative humidity levels while evaluating them with and without the proposed return-air strategy. The controller adapted between humidity and CO_2-critical conditions during run-time. The fresh-air mass flow requirements reduced with increasing difference between the setpoint and ambient vapor mass fractions under humidity critical conditions, and plateaued at 10 g/s where CO_2 was more critical. The proposed strategy provided energy savings ranging from 9% to 34% depending on the operating condition.

1. Introduction

About 25% of green-house gas emissions from road transport in the European Union (EU) have been attributed to heavy-duty vehicles [1]. Battery electric vehicles (BEVs) are viewed as potential low/zero-emission vehicles that can reduce the carbon footprint of road vehicles but it is important for vehicle manufacturers to increase their range under all operating conditions for customer acceptance.

Low ambient temperatures have a significant impact on the energy efficiency and range of electric vehicles [2–4], with cabin climatization being one of the largest auxiliary loads. A heating ventilation and air conditioning (HVAC) system is necessary to ensure safe driving by defogging and defrosting the windshield, and to provide thermal comfort for the passengers. In conventional internal combustion engine vehicles, waste heat energy is used from the engine whereas in BEVs, energy is derived through secondary heaters resulting in range reductions of over 50% [4].

Since a large amount of energy is required to climatize the cabin, it is important to optimize the HVAC systems and the cabin, without sacrificing thermal comfort. In general, the solutions for improving the efficiency of cabin climatization can be divided into two: methods to reduce the energy requirement such as localized zonal conditioning, reflective glazing, thermal insulation, recirculating cabin air, and so on [5–9], and methods to increase the efficiency of the HVAC systems to provide the required energy such as the use of waste heat recovery systems and heat pumps [10–14].

The two main parameters to be considered while recirculating air in the cabin are CO_2 concentration and humidity. Many studies have investigated the recirculation or return-air ratio's (RAR) influence on CO_2 concentration in the vehicle cabin. ASHRAE's accepted CO_2 exposure level in conditioned spaces is about 1000-1200 ppm [15]. Mathur [16] investigated the buildup of CO_2 when operated in RAR-mode and found that the occupants experienced fatigue and tiredness on prolonged exposure. A simplified vehicle cabin was simulated in CFD by

☆ This document is the result of the research project funded by the Swedish Energy Agency/FFI project number, P48024-1.
* Corresponding author.
E-mail addresses: anandh.rameshbabu@chalmers.se (A. Ramesh Babu), simone.sebben@chalmers.se (S. Sebben), zenitha.chroneer@volvo.com (Z. Chronéer), sassan.etemad@volvo.com (S. Etemad).

https://doi.org/10.1016/j.ijheatmasstransfer.2023.125056
Received 2 October 2023; Received in revised form 1 December 2023; Accepted 6 December 2023
Available online 14 December 2023

Nomenclature

Abbreviations

BEV	Battery electric vehicle
CFD	Computational fluid dynamics
CHT	Conjugate heat transfer
HVAC	Heating ventilation and air-conditioning
JOS-3	Joint system thermoregulation model
PMV	Predicted mean vote
PPD	Predicted percentage of dissatisfied
RANS	Reynold's Averaged Navier-Stokes equations
RAR	Return-air ratio

Symbols

R_{th}	Thermal resistance	m^2K/W
y	Thickness of material	m
λ	Thermal conductivity of material	W/mK
P_{sat}	Saturation pressure	Pa
P_0	Reference pressure	Pa
T	Temperature	K or °C
Sc	Schmidt number	-
Le	Lewis number	-
ν	Kinematic viscosity	m^2/s
D	Diffusion coefficient	m^2/s
α	Thermal diffusivity	m^2/s
C	Heat capacity of a node in JOS-3	kJ/K
t	Time	s
Q_{HP}	Heat production	W
Q_B	Heat exchange by blood flow	W
Q_{HC}	Heat exchange by heat conduction	W
Q_{SHL}	Sensible heat loss	W
Q_{LHL}	Latent heat loss	W
T_{sk}	Skin temperature	K or °C
T_o	Operative temperature	K or °C
R_t	Sensible heat resistance	m^2K/W
A	Area	m^2
R_{cl}	Clothing resistance	m^2K/W
f_{cl}	Clothing area factor	-
h_c	Convective heat transfer coefficient	W/m^2K
h_r	Radiative heat transfer coefficient	W/m^2K
E_{sk}	Evaporative heat transfer at the skin	W
w	skin wettedness	-
E_{max}	Maximum heat transfer due to evaporation	W
ϕ	Relative humidity	%
R_{et}	Evaporative resistance	$kPa{\cdot}m^2/W$
L_R	Lewis rate	K/kPa
i_{cl}	Vapor permeation efficiency	-
T_{cl}	Clothing temperature	K or °C
$h(y^+)$	Heat transfer coefficient at a given y^+	W/m^2K
ρ	Density	kg/m^3
c_p	Specific heat capacity	kJ/kg·K
u^*	Velocity scale in the near-wall region	m/s
T^+	Non-dimensional temperature	-
T_w	Wall temperature	K or °C
$T_{o_{CFD}}$	Operative temperature from CFD	K or °C
$\dot{q}''_w$	Wall heat flux	W/m^2
h_{fg}	Latent heat of evaporation	J/kg
$\dot{m}''$	Vapor mass flux	kg/s
e	PI-controller error	-
dt_{co}	Co-simulation time step	s
Q_{heater}	HVAC Heater rate	W
$\dot{m}_{in}$	Inlet mass flow rate	kg/s
γ	Return-air ratio	-
T_∞	Ambient temperature	K or °C
ϕ_∞	Ambient relative humidity	%
k_p, k_i	Gains of the PI-controller	-
α	CO_2 concentration	ppm
ω	Specific humidity	kg of vapor/kg of dry air
x_ω	Vapor mass fraction	-
a, c	Tuning parameters of the humidity controller	-
$T_{g,min}$	Minimum interface temperature between the windows and cabin air	K or °C
Δx_ω	Difference between setpoint and ambient vapor mass fractions	-
v_{veh}	Vehicle speed	km/h
h_{ext}	External heat transfer coefficient	W/m^2K

Subscripts

i	Layers or segments
j	Nodes
k	Step index
set	Setpoint for the corresponding quantity
REC	Mass-averaged quantity from the REC outlet
cab	Mean quantity in the cabin
∞	Ambient condition
bo	Upstream condition to the heater
in	Inlet condition of a quantity

Chang et al. [17] with varying number of occupants and mass flow rate into the cabin. The results were presented as fresh-air requirements of approximately 9 g/s and 3.6 g/s per passenger to maintain 1000 ppm and 2000 ppm of CO_2, respectively. Wei et al. [9] tested a feedback control for the recirculation ratio based on the concentration of CO_2 and showed that the degree of recirculation was inversely proportional to the number of passengers.

In winter, the HVAC system operates in the no-recirculation mode due to the risk of windshield fogging, since the default recirculation option typically sets a high RAR. Shikate et al. [18] proposed a two-layer HVAC, where fresh and recirculated streams were not mixed. They were separately heated and supplied, with the fresh air discharged to the defrosters, and the recirculated air was discharged to the floor outlets. Hirai et al. [19] were among the pioneers of using recirculation control with anti-fog measures and demonstrated energy savings of about 30%. Wei et al. [9] studied different recirculation levels at 0 °C and recommended not to use RAR when a vehicle had more than three passengers. Zhang et al. [8] investigated the use of recirculation at various operating conditions and demonstrated up to 40% energy savings at steady-state. They employed a continuous anti-fog air curtain to help operate at appropriate conditions which considered the windshield temperature and the dew-point of the air from the HVAC unit. Lorenz [20] analyzed several discrete recirculation ratios, and showed that an RAR of more than 50% caused fogging at -10 °C and 70% relative humidity with two passengers in the vehicle. An optimized configuration was proposed with 50% RAR, heated windows, panels and seats, with reduced setpoint for air temperature that resulted in about 57% energy savings. Pan et al. [21] considered both CO_2 and humidity using a simplified thermal model, and employed the strategy which required higher fresh-air intake.

Internal combustion engine-driven trucks typically have high heat output from the engines, and the energy for cabin heating has usually been available. With the advent of electrified trucks, this is not the case. More investigations on various strategies are necessary to reduce its energy expenditure while maintaining good interior climate. While several studies have identified recirculation to be energy efficient, none

have defined a strategy for instantaneous RAR estimation in a transient scenario, nor have they used high-fidelity CFD simulations with a thermoregulation model to estimate realistic vapor sources for recirculation control. In the present work, efforts were made to model an adaptive feedback-based recirculation control for an electric truck cabin, operating in cold weather. High-fidelity CFD simulations were performed with a manikin at the driver's position. A co-simulation procedure between CFD and JOS-3 thermoregulation model [22] was adopted with the consideration of respiration and sweating from the driver to account for realistic moisture production in the cabin. The results from the simulations with the adaptive RAR strategy were compared to operating in no-recirculation mode. A sensitivity analysis was performed by varying the ambient temperature, the relative humidity and the driving speed to investigate the effect of each parameter on the RAR strategy and energy savings. Finally, the effect of number of occupants and the HVAC inlet mass flow rate were analyzed based on the analytical solution for recirculation.

2. Methodology

2.1. Vehicle geometry and CFD setup

The CFD simulations were performed in the commercial solver, STAR-CCM+. A simplified full-scale electric truck cabin was used in this study which included interior cabin air and solids, Fig. 1a. The consideration of the solids (S1-S10), especially the windows (S1 and S2) were important for accurate estimation of RAR.

2.1.1. Cabin solids

The cabin solids are grouped (and colored) based on the material properties (given in Table A.1.1). To model the heat transfer from the cabin air to the ambient, the inner solid surfaces were set up with conjugate heat transfer (CHT) interfaces, while the outer solid surfaces employed a convective boundary condition, which included a heat transfer coefficient (h_{ext}), ambient temperature (T_∞) and a thermal resistance (R_{th}) between the cabin solid and external wall of the truck, as shown in Fig. 1b. The heat transfer coefficient on the external wall of the truck was estimated based on external flow CFD simulations, as explained in Appendix A.2.

The thermal resistance (R_{th}) between each cabin solid and the external wall of the truck was obtained using Fourier's law of heat conduction through multiple layers where the total resistance of the walls is computed using,

$$R_{th} = \sum_{i=1}^{N} \frac{y_i}{\lambda_i} \tag{1}$$

where y_i is the thickness of layer i and λ_i, its thermal conductivity. The thicknesses were measured during an experimental campaign, and the thermal conductivities were estimated from literature. Few cabin solids such as the windshield, side windows, and the exterior doors were in direct contact with the external air and, hence, their thermal resistances were 0 K/W. The seats were considered not to conduct heat to the ambient while the inner and mid-door panels, and the air gap were included in the simulations. Table 1 describes the net thermal resistance imposed on the outer solid surface in the numerical model. The surface-to-surface radiation model was employed to simulate radiative heat transfer in the cabin. The transmissivity, reflectivity, and emissivity of the semi-transparent boundaries were set to 0.5, 0.36 and 0.14, respectively, whereas for the opaque surfaces, 0, 0.2 and 0.8 were used, respectively [23].

2.1.2. Cabin air

The air volume from the air distribution ducts was considered as shown in Fig. 2a. The HVAC system was located on the passenger side, but not included in the simulations. The cabin had six inlets leading to

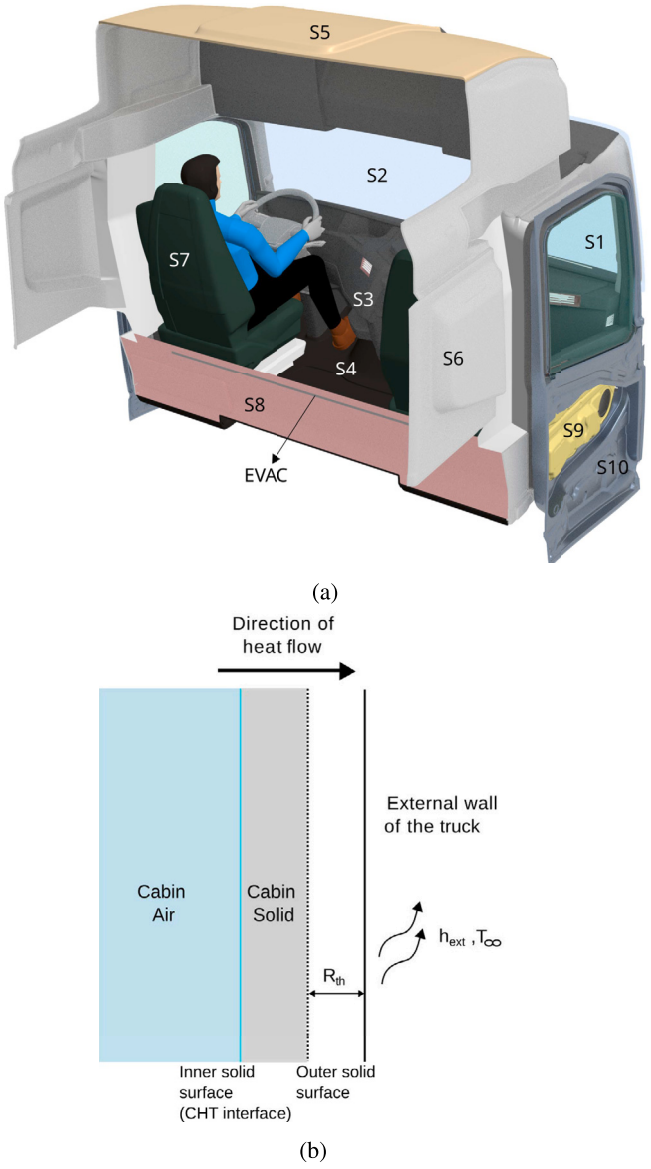

Fig. 1. (a) Truck cabin with all the interior solids (S1-S10) colored based on the corresponding material property from Table A.1.1, along with the evacuation outlet (EVAC) (For interpretation of the colors in the figure(s), the reader is referred to the web version of this article.); (b) Schematic of the boundary conditions on the cabin solids.

Table 1
Thermal resistance on the outer surface of the solids.

Solids	Thermal resistance (K/W)
Windshield, side windows Seat, door (all layers)	0
Floor	0.96
Roof	0.08
Top storage covers	18.13
Rear wall	2.40
Motor wall	1.07
Bunk, bunk lower wall	33.01
Side panels	3.28

a central defroster, vents, and two floor outlets and two side demisters, each with its own inlet surface through which air enters the domain. Fig. 2b illustrates the inlets (in pink) through the doors, air curtains, fed from the floor ducts. Warm air through these inlets reduces window fogging and improves comfort at low ambient temperatures. Two out-

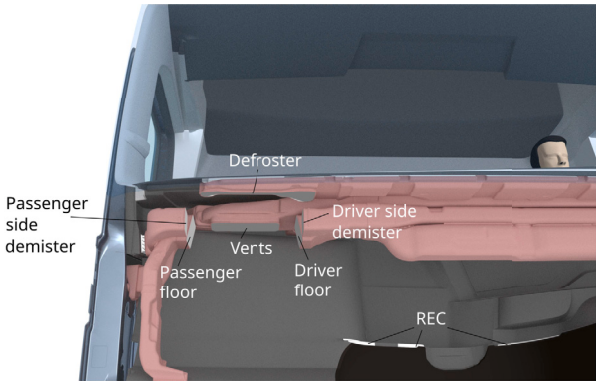

(a)

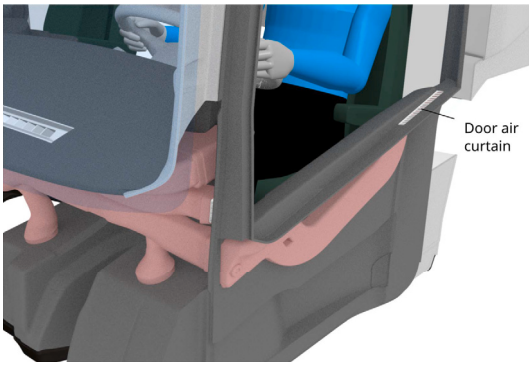

(b)

Fig. 2. Representation of (a) Inlets in the cabin and the recirculation outlet (REC); (b) the door inlets fed from the floor ducts.

lets were considered: a recirculation (REC), Fig. 2a, that led back to the HVAC system, and an evacuation (EVAC), Fig. 1a.

As mentioned, one of the objectives of the study is to understand the influence of moisture and CO_2 produced by the driver on the recirculation ratio. To track these in the cabin, air was modeled as a multi-component ideal gas with dry air and water vapor, and CO_2 was modeled as a passive scalar. This strategy was used since the concentration of CO_2 could be tracked while assuming air to be a binary mixture of dry air and vapor. The properties of the air-vapor mixture are available in literature.

The variations in the dynamic viscosity and specific heat of dry air were taken into account using Sutherland's law, whereas for vapor, they were set to 8.89×10^{-6} Pa-s, and 1868 kJ/kg-K, respectively [24]. The mixture properties were defined based on the mass-weighted average of the two species. The Schmidt number[1] (Sc) and Lewis number[2] (Le) determined the air-vapor mixture diffusivity and thermal conductivity and were computed to be 0.61 and 0.85 [24,25]. The Schmidt number for CO_2 was set to 1.14 [26].

The realizable $k-\epsilon$ (RANS) turbulence model was used since it has been shown to be the most robust model for cabin simulations [7,27,28]. Gravity was taken into account to capture buoyancy effects during heating. Solar radiation was not considered since this effect is generally very low in cold weather [2,29].

A simplified fogging model was considered using the fluid-film multiphase model [30], where the film is composed of water. The film was set up as a shell at the interfaces between the windows (S1 and S2 in Fig. 1a) and the cabin air. Table 2 displays the material properties

[1] $\mathrm{Sc} = \frac{\nu}{D}$, where ν is the kinematic viscosity, and D is the diffusion coefficient of the air-vapor mixture.

[2] $\mathrm{Le} = \frac{\alpha}{D}$, where α is the thermal diffusivity.

Table 2
Material property of water in the fluid-film model [24].

Property	Value
Density (kg/m^3)	998
Specific heat (J/kgK)	4180
Thermal conductivity (W/mK)	0.57
Latent heat (MJ/kg)	2.5

of water condensed at the interface [24]. The phase change process involving evaporation and condensation of water is governed by the concentration and the saturation pressure (P_{sat}) of vapor in air at a given location. The saturation pressure of vapor represents the maximum partial pressure of vapor in a dry air-vapor mixture for a given temperature. In this work, the Antoine formulation was adopted [30],

$$\frac{P_{sat}(T)}{P_0} = \exp\left(11.949 - \frac{3978.205}{T - 39.801}\right) \tag{2}$$

where P_0 is the reference pressure (1 bar), and T, its temperature in Kelvin.

Since the film model was used to detect the occurrence of fogging, the influence of surface tension was neglected to simplify the physics. The effect of the water adhesion to the surface was modeled by assuming a very high dynamic viscosity for water. This allowed the condensed water to stick to the surface, mimicking the effect that surface tension would otherwise have induced. This approach is valid for the current investigation since the proposed recirculation strategy should not fog the windows.

2.2. Co-simulation between CFD and thermoregulation models

The manikin used in this work was simulated based on the joint system thermoregulation model (JOS-3) [22]. JOS-3 consists of 83 nodes where the manikin is divided into 17 segments. Each segment includes an artery, a vein, a core node and a skin node. The limbs contain superficial vein nodes. The head and the pelvis include additional layers in muscle and fat nodes.

JOS-3 models the heat loss to the ambient as sensible heat losses (Q_{SHL}) consisting of convective (Q_c) and radiative heat transfer (Q_r), and latent heat loss (Q_{LHL}) at the skin and through respiration. The heat balance at each segment can be described as (adapted from [31]),

$$C_{j,i}\frac{dT_{j,i}}{dt} = Q_{HP_{j,i}} + Q_{B_{j,i}} + Q_{HC_{(j-j'),i}} - Q_{SHL_{j,i}} - Q_{LHL_{j,i}} \tag{3}$$

where j is the node, i is the segment, C is the heat capacity, T is the temperature, t is the time, Q_{HP} is the heat production, Q_B is the heat exchange by blood flow, and Q_{HC} is the heat conduction with adjacent tissue j'. The differential equation is solved explicitly in time with the initial temperatures corresponding to their neutral setpoints.

The heat loss terms in the thermoregulation model were obtained from CFD and so, only these terms from the original JOS-3 model and the modifications are explained for completeness. The sensible heat loss from the skin at each step k is computed as,

$$Q_{SHL,i}|_k = \left.\frac{T_{sk,i} - T_{o,i}}{R_{t,i}}\right|_k \cdot A_i \tag{4}$$

where T_{sk} is the skin temperature, T_o is the operative temperature, R_t represents the sensible heat resistance and A, the surface area of the segment.

The sensible heat resistance is defined as,

$$R_{t,i}|_k = 0.155R_{cl,i} + \frac{1}{f_{cl,i}\cdot(h_{c,i}|_k + h_{r,i}|_k)} \tag{5}$$

where R_{cl} and f_{cl} are the clothing resistance and the clothing area factor, h_c and h_r are the convective and radiative heat transfer coefficients. The evaporative heat transfer at the skin (E_{sk}) is defined as,

$$E_{sk,i}|_k = \left(w_i \cdot E_{max,i}\right)|_k \tag{6}$$

where w is skin wettedness and E_{max} is the maximum heat transfer due to evaporation. Skin wettedness is limited between [0.06, 1] and is dependent on the temperature difference between various nodes and their corresponding setpoint temperatures, and a coefficient that factor aging and segment type. At low temperatures, the skin wettedness defaulted to 0.06, which represents low sweating. The term E_{max} is computed as,

$$E_{max,i}|_k = \left.\frac{P_{sat}(T_{sk,i}) - \phi_i P_{sat}(T_{a,i})}{R_{et,i}}\right|_k \cdot A_i \tag{7}$$

where $P_{sat}(T_{sk})$ represents the saturated vapor pressure at the skin temperature, $\phi P_{sat}(T_a)$, the vapor pressure at the air temperature scaled with the relative humidity (ϕ), and R_{et}, the evaporative resistance of each segment. The saturated vapor pressure is calculated using eqn. (2). The evaporative resistance is estimated using,

$$R_{et,i}|_k = \frac{1}{L_R}\left.\left(\frac{0.155 R_{cl,i}}{i_{cl,p}} + \frac{1}{f_{cl,i} \cdot h_{c,i}}\right)\right|_k \tag{8}$$

where L_R is the Lewis rate (16.5 K/kPa), and $i_{cl,p}$ is the vapor permeation efficiency of the clothes (45%).

The co-simulation was performed with the JOS-3 simulated ahead in time by dt_{co}, and the boundary conditions on the manikin were interpolated accordingly in CFD. This approach was employed since the thermal inertia is considerably larger for the human than for the air in the cabin. Consequently, for a small dt_{co}, the variations in segment temperatures would be much less than the variations in the air temperature surrounding the segment. This resulted in the skin and clothing temperatures being computed explicitly in time, based on the heat losses evaluated from CFD, while the heat flux itself was evaluated implicitly in time, based on the variation in the clothing temperatures.

The sensible heat losses were estimated using CFD by multiplying the wall heat flux ($\dot{q}''_{w,i}$) and the area for each segment. The boundary condition for the temperature imposed on the manikin was the clothing temperature (T_{cl}). Assuming a quasi-steady heat conduction through the clothes (the thermal capacitance of the clothes were neglected), the temperature on the clothes of each segment can be computed as,

$$T_{cl,i}|_k = T_{sk,i}|_k - \frac{Q_{SHL,i}|_{k-1}}{A_i} \cdot R_{cl,i} \tag{9}$$

It must be noted that the sensible heat loss is evaluated at the previous step $(k-1)$ for the reason explained above.

Since the sensible heat losses now were solved for, eqn. (4) was no longer employed in the co-simulation for the heat balance equation. Instead, the sensible heat resistance was recomputed for completeness as,

$$R_{t_i}|_k = 0.155 R_{cl,i} + \left.\frac{T_{cl,i} - T_{o_{CFD,i}}}{Q_{SHL,i}}\right|_k \cdot A_i \tag{10}$$

where $T_{o_{CFD}}$ represents the operative temperature that is obtained from CFD. This operative temperature was derived from the wall heat flux and a wall function for the heat transfer coefficient $h(y^+)$. According to [30], the recommended y^+ value is 100 to obtain realistic heat transfer coefficients. The formulation for $h(y^+)$ is,

$$h(y^+) = \frac{\rho c_p u^*}{T^+(y^+)} \tag{11}$$

where ρ is the density, c_p is the specific heat of air, u^* is the velocity scale in the near wall region, and T^+, the non-dimensional temperature obtained using blended wall functions [32]. The operative temperature, $T_{o_{CFD}}$ was computed based on the total wall heat flux (both convection and radiation), and the heat transfer coefficient at the specified y^+ as,

$$T_{o_{CFD,i}}|_k = T_{w,i}|_k - \left.\frac{\dot{q}''_{w,i}}{h_i(y^+)}\right|_k \tag{12}$$

where $\dot{q}''_w$ is the total wall heat flux computed in CFD for a wall temperature T_w. Equation (12) and the second term of eqn. (10) are synonymous where the resulting sensible heat resistance between the environment and the manikin surface is $1/h(y^+)$.

The formulations for the latent heat losses were largely unchanged from the original implementation. The heat transfer coefficient computed in eqn. (11), which was flow dependent, was used in eqn. (8). The evaporative heat transfer leads to formation of water vapor on the skin. Thus, vapor mass flux ($\dot{m}''$) from each segment was computed as [33],

$$\dot{m}''_i|_k = \frac{E_{sk,i}|_k}{h_{fg} \cdot A_i} \tag{13}$$

where h_{fg} is the latent heat of evaporation. The obtained vapor mass flux was introduced as source from the manikin in CFD.

2.3. Control strategy

The two controllers employed were the cabin heater and the return-air ratio controller. To improve the speed of the co-simulation, the controllers were evaluated every dt_{co}.

2.3.1. Cabin heater

The cabin heater was operated with an adaptive proportional integral (PI) controller targeting the HVAC inlet and the mean temperature of the cabin. The inlet mode of the PI controller operated with a setpoint for the inlet temperature ($T_{in,set}$). This was defined as a function of the ambient temperature (T_∞), as $40 - T_\infty$ [°C]. The controller operated in this mode until the mean cabin temperature (T_{cab}) reached 20 °C. Beyond this state, the controller switched to the cabin-temperature mode, with the setpoint for the mean temperature at 22 °C ($T_{cab,set}$). Thus, the error was computed as,

$$e_q|_k = \begin{cases} T_{in}|_{k-1} - T_{in,set}, & \text{if } T_{cab}|_k < 20\,^\circ\text{C}, \\ T_{cab}|_k - T_{cab,set}, & otherwise. \end{cases} \tag{14}$$

$$Q_{heater}|_k = k_p e_q|_k + \sum_{k=0}^{N} k_i e_q|_k dt_{co} \tag{15}$$

where e_q is the instantaneous error, Q_{heater} is the heating load, k_p and k_i are the gains of the controller. The value for k_p was taken as -1 and k_i took the values -5 in the inlet temperature mode, and -0.5 in the cabin temperature mode. When the modes switch, the integral state of the controller was recomputed to provide a smooth transition. Based on the output of the PI controller, the inlet temperature to the cabin was set as,

$$T_{in}|_k = T_{bo}|_k + \frac{Q_{heater}|_k}{\dot{m} c_p} \tag{16}$$

where T_{bo} is the temperature of the air upstream of the heater, $\dot{m}$ is the mass flow rate of air into the cabin and c_p is the specific heat of air. The temperature of air upstream of the heater was defined as,

$$T_{bo,k} = \gamma T_{REC}|_k + (1 - \gamma|_k) T_\infty \tag{17}$$

where γ represents the return-air ratio and T_{REC} is the mass flow averaged temperature obtained at the outlet of the boundary, REC. To prevent overshoot, the maximum temperature at the inlet was limited to the setpoint temperature when operating in the cabin-temperature mode.

2.3.2. Return-air strategy

The return-air strategy employed two controllers, one for CO_2 (α) and the other for vapor mass fraction (x_ω) and chose the most critical strategy.

The concentration of CO_2 at the inlet of the ducts with RAR was defined similarly to eqn. (17) as,

$$\alpha_{bo}|_k = \gamma|_k \alpha_{REC}|_k + (1-\gamma|_k)\alpha_\infty \tag{18}$$

where α_{REC} is the mass flow averaged value entering the REC boundary, and α_∞ is the ambient condition. The equation for x_ω was defined similarly.

The setpoint for CO_2 in this work was considered to be a mean concentration of 1000 ppm to maintain safe operating environment in the vehicle based on previous works [9,17]. The error (e_α) was defined as,

$$e_\alpha|_k = \alpha_{cab}|_k - \alpha_{cab,set} : \alpha_{cab,set} \rightarrow 1000 \text{ ppm} \tag{19}$$

The output of the controller yielded the RAR γ_α, and was formulated analogous to eqn. (15). The gains for the controller were taken from the work of Wei et al. [9] as -0.03 for k_p and -0.0003 for k_i.

The criterion for humidity must be formulated such that the air entering the cabin did not fog the windshield and the side windows. So, if the dew-point temperature of the air from the HVAC is lower than the minimum window temperature ($T_{g,min}$), fogging can be prevented. Thus, the setpoint for vapor mass fraction was defined with a safety margin of 1 °C from $T_{g,min}$. The vapor mass fraction was defined as,

$$x_\omega(T,\phi) = \frac{\omega(T,\phi)}{1+\omega(T,\phi)} \tag{20}$$

where ω is the specific humidity of vapor, defined as,

$$\omega(T,\phi) = 0.622\frac{\phi P_{sat}(T)}{P - \phi P_{sat}(T)} \tag{21}$$

P_{sat} is the saturation pressure obtained from the Antoine equation (eqn. (2)), ϕ is the relative humidity and P is the reference pressure. The setpoint was redefined at each step as $x_\omega(T_{g,min}|_k - 1, 100\%)$.

The saturation vapor pressure is an exponential function of temperature, resulting in large variations of the setpoint for vapor mass fraction. To make the controller robust under all conditions, the gains were set based on the ambient operating condition:

$$k_p(T_\infty,\phi_\infty) = -\frac{(1-\phi_\infty)\left(1+\frac{T_\infty+a}{a}\right)}{\left(x_\omega(T_\infty-1,1) - x_\omega(T_\infty,\phi_\infty)\right)} \tag{22}$$

$$k_i(T_\infty,\phi_\infty) = \frac{k_p(T_\infty,\phi_\infty)}{c(T_\infty,\phi_\infty)} \tag{23}$$

where $\phi_\infty \in [0,1]$, T_∞ described in °C, a and c are tuning parameters. The parameter a was set to 20 while c was set adaptively, and is described in the Appendix A.5. The instantaneous error for the humidity controller was,

$$e_{x_\omega}|_k = x_{\omega,bo}|_k - x_\omega(T_{g,min}|_k - 1, 100\%) \tag{24}$$

The rest of the controller was defined similar to eqn. (15) and the output of this controller yielded γ_{x_ω}.

The minimum of (γ_α, γ_{x_ω}) was considered as the final recirculation ratio (γ) for the subsequent step. This approach is equivalent to the strategy proposed by Pan et al. [21], however the usage of PI controller provides feedback control and aids in maintaining the setpoints despite local flow variations. The output of the re-circulation controller was saturated between [0, 0.95].

It should be mentioned that the gains of the vapor mass fraction controller were obtained based on tuning and benchmarking. The authors acknowledge that the controller can under-perform in some scenarios. However, since the system is non-linear with varying setpoints, a sophisticated form of optimal control would be needed resulting in an extremely expensive simulation approach.

2.4. Assumptions and limitations

The main assumptions and limitations in the current approach are:

- The dashboard and the seats in a real vehicle are complex assemblies with multiple parts and layers. In the CHT model, only the outer shells were included for the dashboard and each seat was taken as a single lumped material.
- The same inlet temperature was used on all the inlet boundaries at a given time, while these temperatures may be different in a real vehicle depending on the operating condition.
- All uncontrolled leakages in the cabin were neglected. This consideration was necessary since leakage occurs at several locations in the cabin and the amount of flow through them was unknown. The amount of leakage is dependent on the vehicle speed, the HVAC blower setting, the vehicle geometry and recirculation employed since they affect pressure difference between inside the cabin and the exterior. Typically, the presence of leakages reduces the concentration of CO_2, vapor and temperature in the cabin and increases the energy consumption [34,35]. Thus, the consequence of assuming no leaks is that the air-quality would be estimated to be worse, i.e. higher CO_2 and vapor concentration, and higher temperatures than a cabin with leakage. This would result in underpredicted return-air ratios and energy consumption.

2.5. Simulation framework

A summary of the coupling of CFD, JOS-3 and the controllers is described in Fig. 3. The co-simulation was set up with an update interval (dt_{co}) of 1 s. At each step, JOS-3 was computed for 1 s, and the new boundary conditions in the form of surface temperatures and vapor fluxes from the manikin segments were imported to the CFD simulation. These conditions were then interpolated in time for smooth transition in CFD. At the end of the JOS-3 execution, the controllers were evaluated based on subsection 2.3 and the new heater load and RAR were revised in the CFD model. The scripts used to perform the co-simulation are available in https://github.com/anandhSRB/thermRegCtrl.

2.5.1. Boundary conditions

Several boundary conditions needed to be defined for the co-simulation. For clarity, these conditions are grouped into CFD-based, thermoregulation-based, and case-based conditions. Each category includes a number of constants and a few scenario-dependent variables.

CFD-based conditions

- Mass flow rate into the cabin from the blower: 0.083 kg/s
  1. Defroster: 0.0166 kg/s
  2. Vents: 0.0099 kg/s
  3. Driver-side demister: 0.0074 kg/s
  4. Passenger-side demister: 0.0074 kg/s
  5. Driver floor: 0.01826 kg/s
  6. Passenger floor: 0.0232 kg/s
- Mass flow rate from the human nostrils: 9 l/min [17]
- Ambient CO_2 concentration: 420 ppm
- Human breath CO_2 concentration: 40000 ppm
- Relative humidity of human breath: 90% [36]. The vapor mass concentration was computed based on eqn. (20) and eqn. (21) at the core temperature of the driver's head during runtime.

The air temperature, mass fractions of vapor and dry air, and the CO_2 concentrations were defined as functions at the inlet boundaries based on eqn. (16), and eqn. (18) and corresponding variations for vapor and air mass fraction. The cabin was initialized to the same temperature, vapor and CO_2 concentration as the ambient. The boundary conditions for driving speed, ambient temperature and relative humidity are explained later in the subsection, case-based conditions.

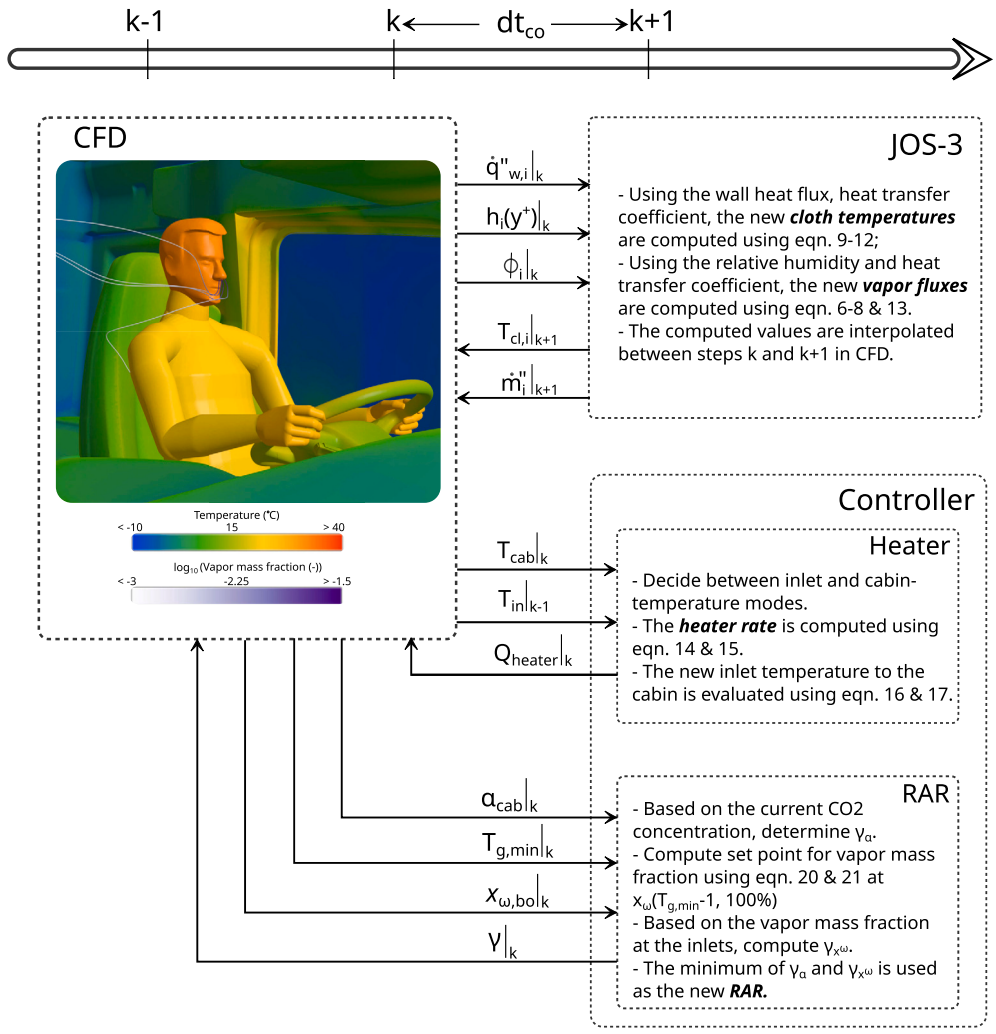

Fig. 3. Simulation framework describing the co-simulation of CFD, JOS-3 and the controllers.

Table 3
Parameters and values considered in the sensitivity study.

Parameter	Values
Vehicle speed (km/h)	0, 30, 60, and 90
Ambient temperature (°C)	-20, -10, and 0
Relative humidity (%)	50, 70, and 90

Thermoregulation-based conditions

- Initial soak time (t_{soak}): 5 min. This was imposed to get a representative initial skin temperature for the driver under a certain ambient condition.
- Clothing resistance: see Appendix A.3.
- Physical activity ratio: 1.6. The ratio of total energy production to the metabolic rate of the driver.

Case-based conditions and sensitivity analyses Each co-simulation was defined using three parameters: the vehicle speed, the ambient temperature and its relative humidity. These parameters were chosen since they had the largest influence on the choice of recirculation strategy, energy consumption and thermal comfort. To understand their impact, a reference case at 90 km/h, -10 °C and 70% relative humidity was considered. From the reference case, one parameter from Table 3 was varied at a time. To quantify the reduction in energy expenditure using recirculation, the cases were also investigated without recirculation, i.e. $\gamma = 0$.

2.6. Mesh and time step analyses

The mesh and time step analyses were done in three stages. Firstly, a pre-mesh study was performed with four meshes without energy transport and JOS-3 coupling, using steady-state flow model. A suitable mesh was chosen, and a time-step sensitivity analysis was then performed at four time steps, with the JOS-3 coupling. Finally, a combined mesh and time step sensitivity to the solution was investigated. For the second and third steps, the cases were evaluated based on the performance of the JOS-3 model under co-simulation, the controller strategy and the temperature transport in the cabin.

2.6.1. Pre-mesh study

Four meshes with 16 million, 23 million, 33 million and 48 million cells were studied. The meshes were obtained by refining globally while maintaining a wall $y^+ \approx 1$ with a prism layer growth rate of 1.35 on all surfaces. In this study, three parameters were compared: Mean skin friction coefficient on different manikin segments, velocity magnitude and turbulent kinetic energy along two vertical line probes at the driver and passenger positions. The configurations are denoted as Mesh-1 to Mesh-4 in the descending order of cell count.

From the mean skin friction coefficient, Fig. 4a, it can be seen that the Mesh-4 deviates from the finer meshes on many segments. Fig. 4b

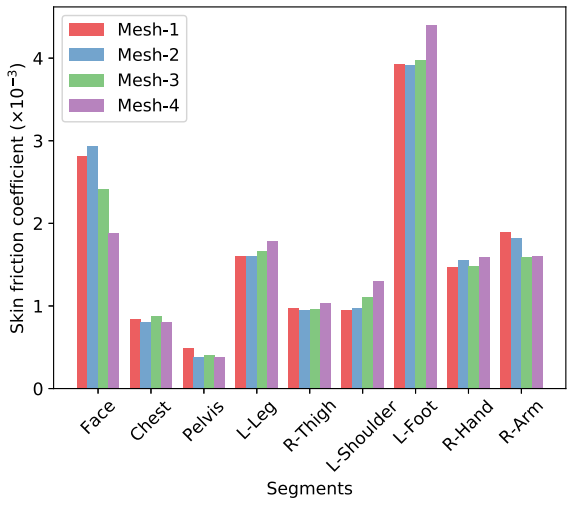

(a)

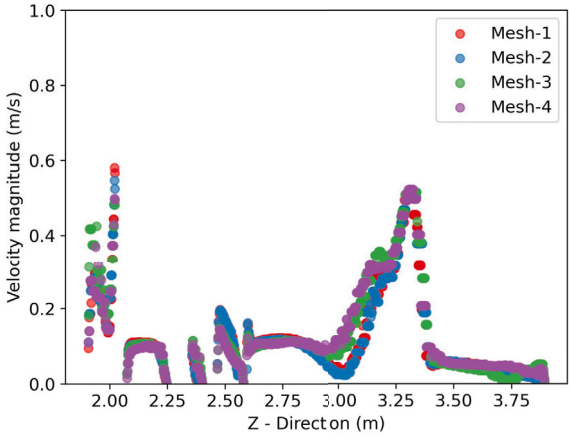

(b)

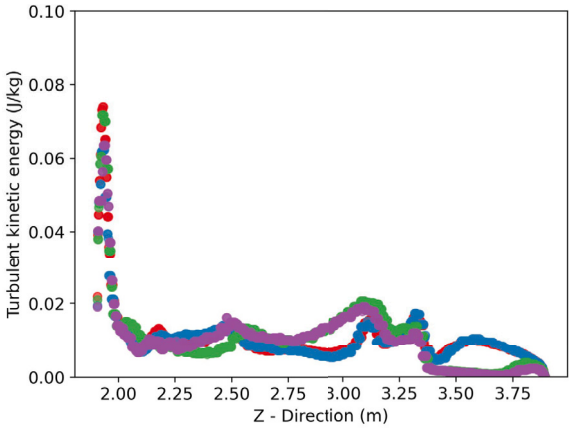

(c)

Fig. 4. Results of the pre-mesh study: (a) Mean skin friction coefficient of selected segments on the manikin; (b) Velocity magnitude along the driver line and (c) Turbulent kinetic energy along the passenger line.

displays the velocity magnitude along the driver line and Fig. 4c, the turbulent kinetic energy along the passenger line. From these plots, it can be seen that all meshes produce similar velocity magnitudes and turbulent kinetic energy profiles, with Mesh-3 and Mesh-4 deviating the most from the finest mesh. Based on these results, Mesh-2 was used

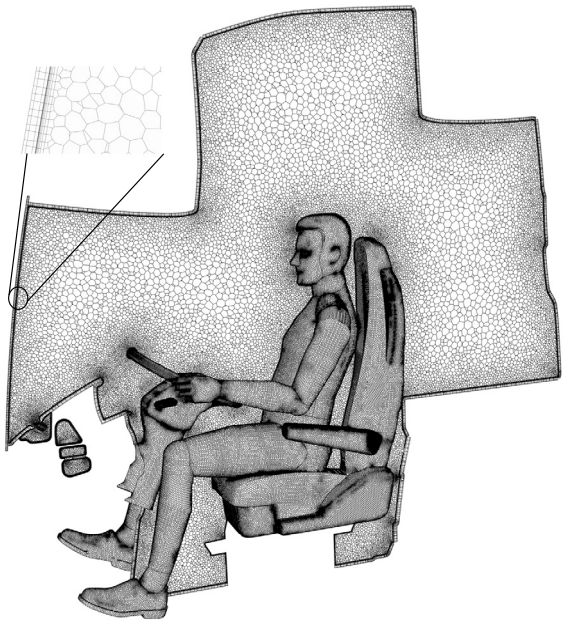

Fig. 5. An XZ-mesh section along the driver's median plane with a zoomed image of the prism layers close to the front windshield.

for further investigations. The resulting surface mesh on the manikin and a section of the volume mesh along the driver's median plane are presented in Fig. 5.

2.6.2. Time-step study

The outputs of the JOS-3 are dependent on the wall heat flux ($\dot{q}''_w$) and heat transfer coefficient ($h(y^+)$) exported from CFD for each manikin segment. Using the UCB-Zhang comfort model [37], the local and overall sensations and comfort can be estimated. Since they are dependent on the segment and core temperatures, and their variations in time, the overall thermal sensation, which is a weighted average of local thermal sensations, was used as a proxy for the interaction between CFD and JOS-3. Additionally, the recirculation controller targets the concentration of CO_2 in the domain and vapor mass fraction at the inlet, and the heater is dependent on mean cabin temperature transport. Hence, the vapor mass fraction at the inlet and the average cabin temperatures were also compared.

Four time-steps (0.5 s, 0.2 s, 0.1 s and 0.05 s) were simulated with the same settings as the reference case, i.e., driving at 90 km/h, at -10 °C, and 70% relative humidity for 10 min. Fig. 6 displays the results of the time-step sensitivity study. The time-steps 0.05 s, 0.1 s produced identical results with 0.2 s showing slight deviations. The largest time-step of 0.5 s under-predicted the average cabin temperature and under-estimated the other transport quantities, which results in more aggressive control strategies. Thus, time step 0.2 s was chosen as it provided the best compromise between simulation time and accuracy.

2.6.3. Combined mesh and time-step study

The chosen setup (Mesh-2 and 0.2 s) was evaluated against finer combinations (i.e. Mesh-1 with 0.1 s, Mesh-1 with 0.2 s, and Mesh-2 with 0.1 s). This was done to ensure that the results had low variation to Courant number with mesh and time-step changes. The vapor mass fraction at the inlets, Fig. 7 demonstrates the low mesh and time step dependency of the transported quantities. Hence, Mesh-2 with 0.2 s was considered to be sufficiently accurate to capture the transport of various quantities in the cabin, and provide feedback to the controllers to function effectively.

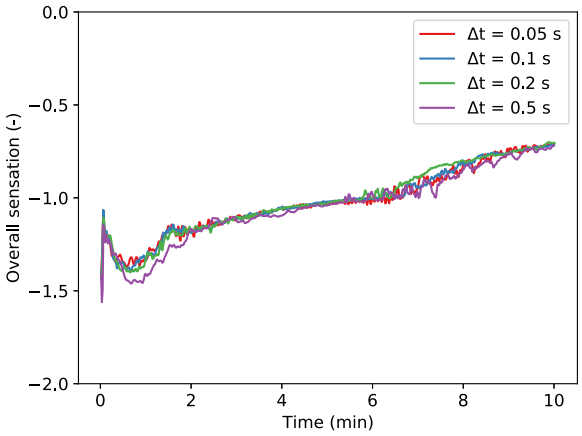

(a)

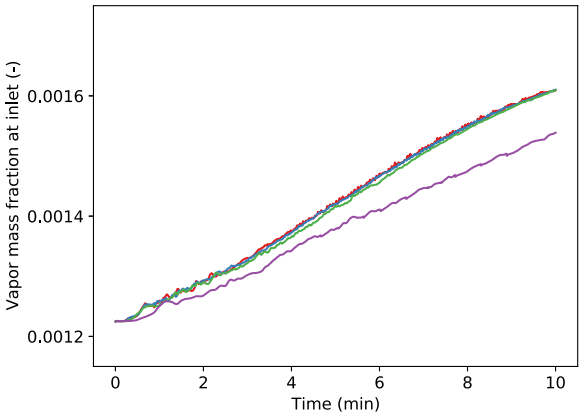

(b)

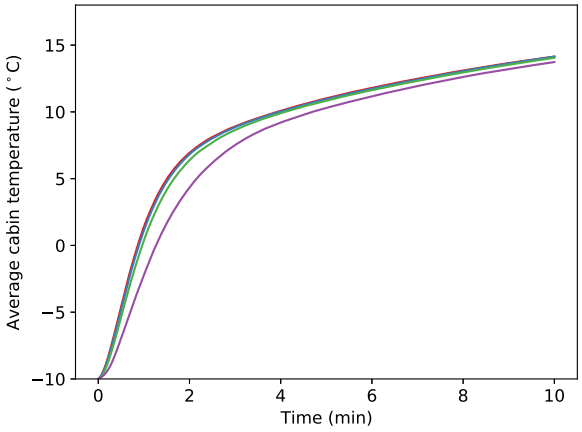

(c)

Fig. 6. Results of the time-step sensitivity study: (a) Overall sensation; (b) Vapor mass fraction at the inlet and (c) Average cabin temperature.

2.7. CFD model validation

The results from a climatic chamber test performed on the truck at stand-still conditions without a manikin, were used to validate the accuracy of the CFD model. The truck cabin was fastened with several thermocouples, as specified in Table 4 and shown in Fig. 8. The thermocouples, Driver-left, Driver-right, Passenger-left and Passenger-Right measure the air temperatures at the head level while the others measure the surface temperatures. During the test, the cabin was soaked to an ambient temperature of 0 °C (T_∞) and was heated for two hours with the Auto-HVAC setting and a target of 22 °C. The temperatures at the end of the test were monitored for about 10 minutes to ensure they reached steady values. For effective comparison with the experimental data, a steady-state numerical simulation was performed with Mesh-2 (without the manikin), and the results are shown in Fig. 9. It can be seen that they agree well with each other with several estimations from the numerical simulation within the probe's accuracy of ± 0.5 °C. Although small deviations are seen for certain probes, the model was considered validated since the mean error was 2.5% and the maximum error was about 6.5% for the considered case.

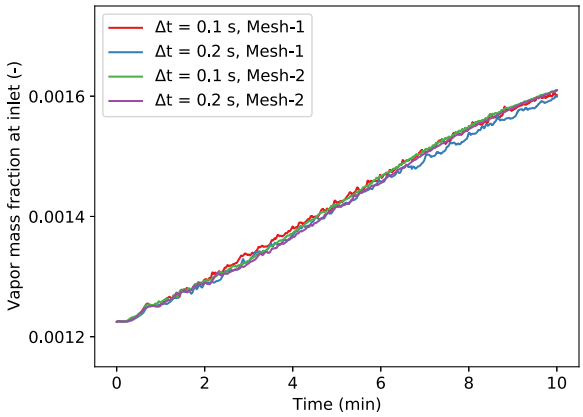

Fig. 7. Sensitivity of the vapor mass fraction at the inlet to finer mesh and time-step configurations.

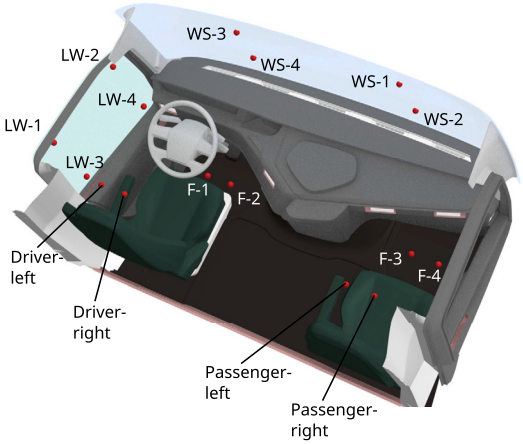

Fig. 8. Positioning of the thermocouples during tests in the climatic chamber.

Table 4
Specifications of the thermocouple used in the experiments.

Thermocouple	Measuring Range	Accuracy
K-type	-50 °C to 200 °C	±0.5 °C

3. Results and discussions

3.1. Co-simulation results of the reference case

Fig. 10 shows the mean velocity magnitude along the driver's median plane and isosurfaces where the velocity is greater than 0.75 m/s for the reference case with RAR-control. The isosurfaces illustrate the region where the flow enters the cabin. Due to low mass flow rate

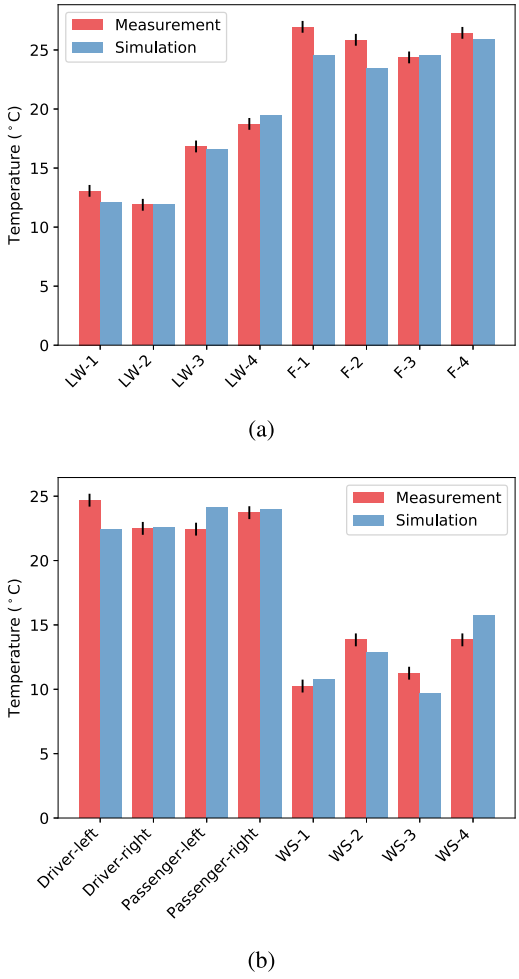

Fig. 9. Comparison of the thermocouples' temperatures from the numerical simulation and experiment. The uncertainty of the experiments was considered to be the probe's accuracy. (a) Left window and floor thermocouples; (b) Head-level air temperature and front windshield thermocouples.

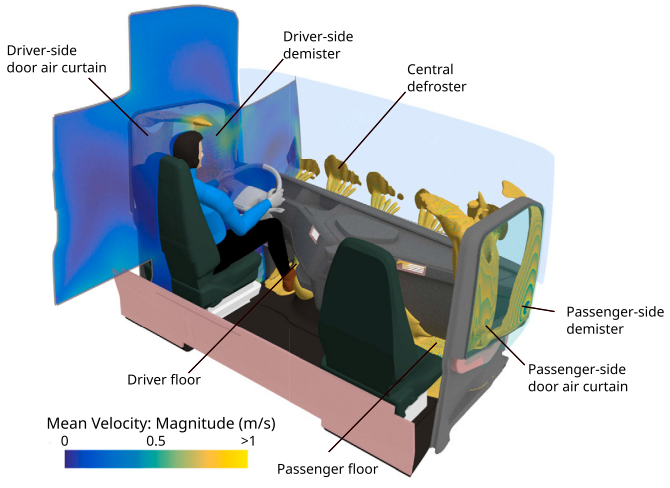

Fig. 10. Mean velocity magnitude along the driver's median plane and isosurfaces of velocity with values greater than 0.75 m/s.

through the vents, the flow from the corresponding inlet was not captured. The main energy source to heat up the cabin is the heater modeled at the inlet and, therefore, a strong convection effect is seen in these regions. This is visualized in Fig. 11, where the temperature along the driver's median plane and front window, along with the boundary heat flux on the driver is displayed at several times during the heat-up. At 10 s, a plume of warm air rises from the driver, denoting natural convection owing to the high surface temperature. This disappears when the inlet flow enters the cabin as seen in the subsequent images. The local variations in the temperature distribution along the plane can be attributed to the convective jets from the inlet flow, in addition to respiration from the manikin. Due to the large temperature difference between the driver and the cabin air, a large heat flux is seen at the beginning, and it gradually reduces as the cabin warms up. The flow from the central defroster warms the front window. However, due to the high driving speed of 90 km/h, the windshield remains cold, away from the region where the defroster flow is incident.

In regard to the results from thermoregulation model, Fig. 12 illustrates the variation in the local skin temperatures versus time for 30 min at selected segments on the manikin. At the start, the skin temperatures are representative of 5 min soak at the respective operating condition. As seen, they decrease for a short duration due to cold air being forced on the driver, accelerating the heat loss. As the cabin warms up, the skin temperatures rise gradually everywhere, except on the right hand.

The average convective and radiation fluxes on the selected segments are shown in Figs. 13a and 13b. It can be seen that the heat losses decrease with time due to the cabin heating up. Most of the segments have about -70 to -100 W/m^2 combined heat flux (sum of convective and radiative), while for the Head, R-Foot, and R-Hand, they vary. This effect stems from the low clothing resistances imposed (Table A.3.1) and the local flow interactions with the manikin. Similar trends were observed for L-Hand, though not shown here. After about 10 min, the R-Foot experiences a positive convective heat flux. This is because of a hot air-jet from the floor-inlet striking it as the heaters engage completely, creating a hot-spot, illustrated in Fig. 14. This was however not seen for the L-Foot.

Fig. 15a and 15b display the local sensation of the segments and the overall sensation/comfort based on the UCB-Zhang thermal comfort model. All segments, except the pelvis and neck, feel cold (<-1) until about 5 min. The hands and the feet feel cold even at the end of the simulation. This is indicative of insufficient clothing insulation under these conditions. Although not considered in this study, this result also exhibits the necessity of steering heaters in cold weather. The neck has a high local sensation since it was considered to be a part of the torso, and the imposed resistance was too high resulting in high skin temperature. The overall sensation (Fig. 15b) is a weighted average of the local sensations and it shows that the conditions are close to neutral (around zero) at the end of the simulation, with the majority of the time being greater than -1. The overall comfort is the mean of the two lowest and the highest local comforts, and shows that the conditions are uncomfortable during the entire simulation time. The differences in sensation and comfort between control strategies will be discussed at the end of the subsection.

Fig. 16 presets the vapor mass fraction at the inlet, and RAR for the case with adaptive control on the reference case. It can be seen that the controller operates as expected by varying the RAR to achieve the required setpoint as shown in Fig. 16a. The dotted and dashed lines in the figure represent the variation in the vapor mass fractions that cause fogging and the corresponding the setpoint from the controller, which takes the minimum temperature of the interface into account. As shown in Fig. 11, the windshield remains quite cold far from where the defroster flow is incident due to the high driving speed in this case. There is little over-shoot in the control, indicating that the operating conditions at the inlet never exceed the saturated state on the front window. The resulting RAR is about 78% after 30 min and this is expected to increase with rising minimum window temperatures. The mean cabin CO_2 concentration with this RAR was 775 ppm, which indicates that the humidity is the more critical of the two parameters for RAR control. With the RAR-strategy, the total energy consumption was approximately 6.3 MJ over the 30 min of the simulation, which is about 29.3% lower than the same

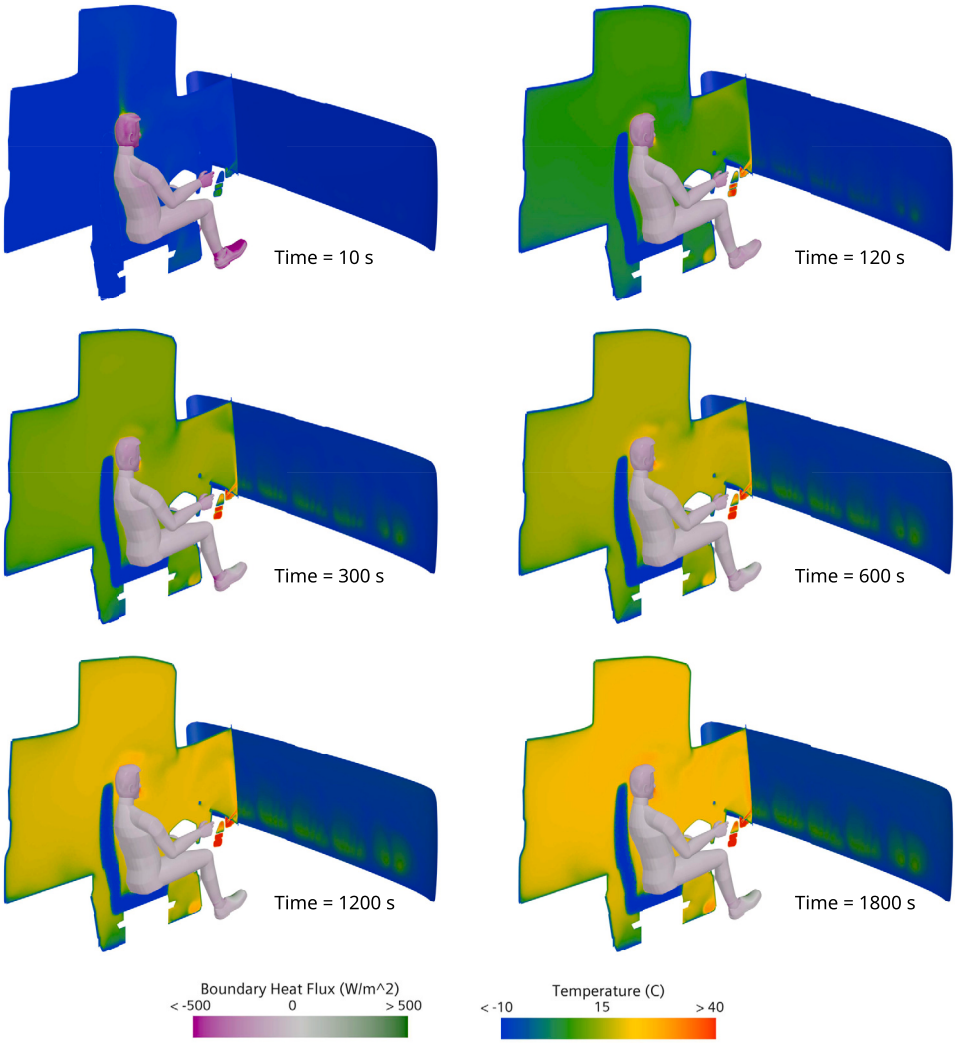

Fig. 11. Temperature distribution along the driver's median plane and front window along with the boundary heat flux on the driver at several time instances during the heat-up.

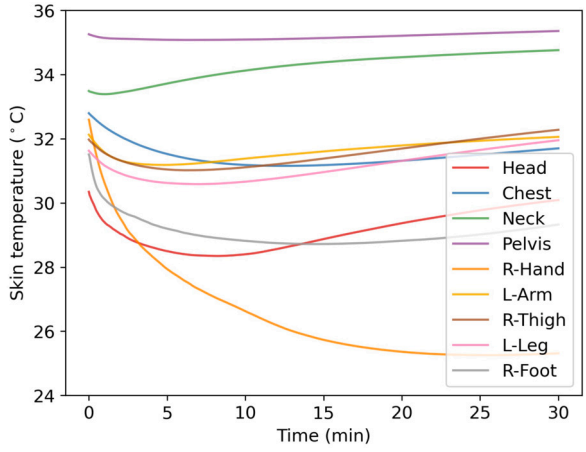

Fig. 12. Variation in the skin temperatures of selected segments from JOS3-CFD co-simulation.

scenario with no recirculation. The average temperature of the cabin with the RAR is about 0.5 to 1 °C lower than the case without recirculation, as displayed in Fig. 17. This is because the heater-rate drops due to the hot air entering the recirculation outlets under the dash-panels. A large portion of the air from the floor inlets moves towards the REC ducts upon striking the foot of the driver, and/or the floor of the truck. This means that the hot air from the inlets do not mix with the cabin and less energy is imparted for the purpose of cabin heating. However, this did not severely affect the overall thermal sensation and comfort of the driver as shown in Fig. 15b.

3.2. Results from the parametric study

The results from section 3.1 demonstrated the feasibility of the RAR as a means to reduce energy consumption. In this subsection, the operating conditions entailing the vehicle speed, ambient temperature and relative humidity are varied according to Table 3 to analyze their effect on the control strategy and energy consumption.

3.2.1. Effect of varying vehicle speed

The effect of vehicle speed was studied while keeping the ambient temperature at -10 °C and 70% relative humidity. The vehicle speed greatly influences the heat loss from the vehicle as the external heat transfer coefficient is a function of the Reynold's number under driving conditions. The windows are in direct contact with the ambient air, and thus, the minimum interfacial temperature between the cabin air and

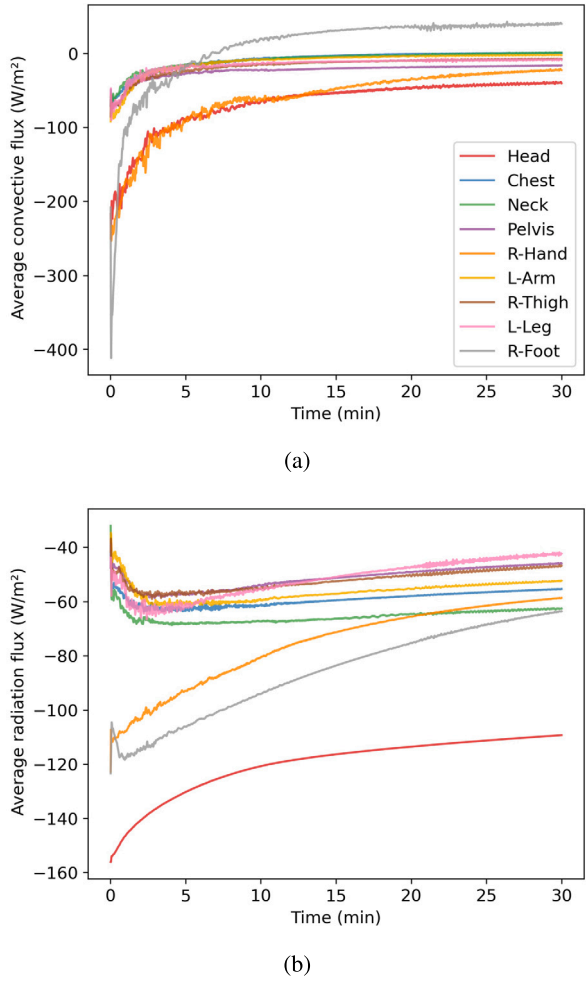

Fig. 13. Heat flux from CFD (a) Convective heat flux; (b) Radiative heat flux.

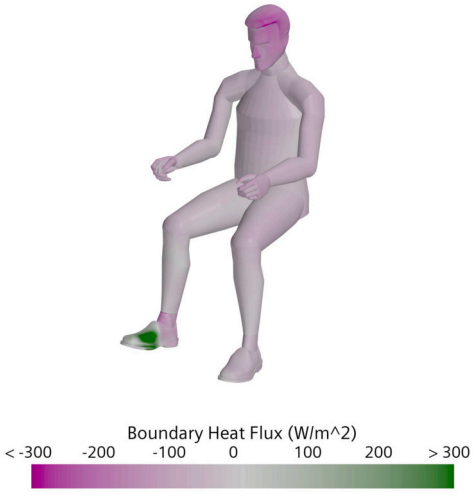

Fig. 14. Boundary heat flux on the human.

the windows, which is used to generate the setpoint for the humidity controller (see Fig. 3), is largely dependent on the driving speed.

Fig. 18 displays the temperatures of inner windshield surface at 30 min under different speeds. It can be seen that at higher speeds the temperatures are quite low due to high heat transfer, while at 0 km/h, the external heat transfer is natural convection dominated as explained

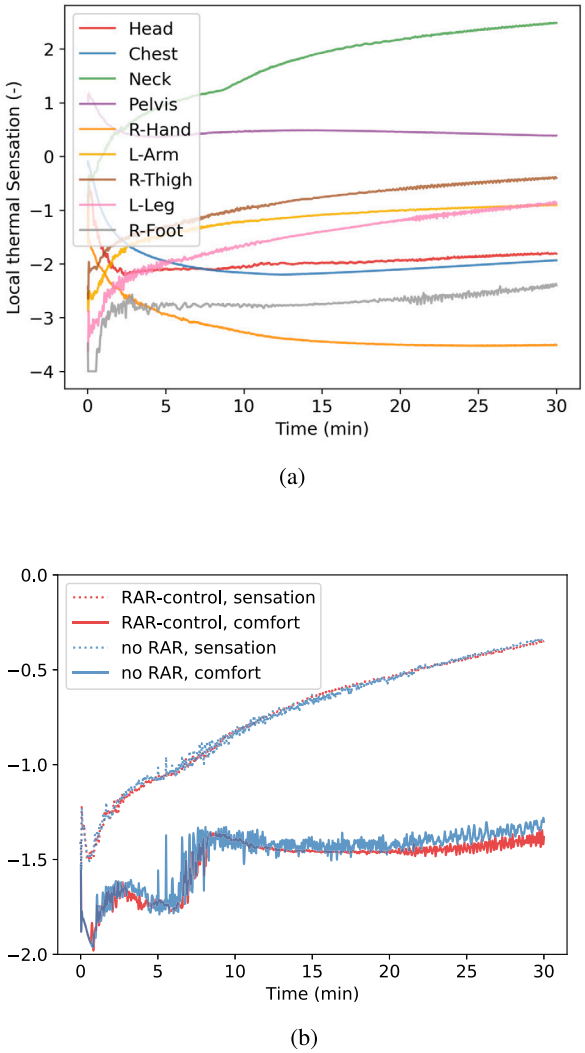

Fig. 15. Thermal comfort metric of the driver based on UCB-Zhang comfort model: (a) Local thermal sensations on selected segments; (b) Overall thermal sensation and comfort comparing scenarios with and without recirculation.

in Appendix A.2. Consequently, the rate of increase in the cabin temperature is inversely proportional to the vehicle speed. Additionally, the higher window temperatures at lower speeds, result in lower radiation losses from the manikin. Thus, the overall thermal sensation is also higher at lower speeds as shown in Fig. 19. The cabin requires about 19 min at stand-still to reach 20 °C, while the same temperature is achieved in 24, 26 and 28 min at 30, 60 and 90 km/h, respectively.

Figs. 20a and 20b display the vapor mass fraction at the inlet and the mean CO_2 concentration in the cabin, respectively. The results can be classified into driving (30 km/h, 60 km/h and 90 km/h) and stand-still (0 km/h) cases. As the windshield heats up, the setpoint for vapor mass fraction at the inlet increases but at different rates for each vehicle speed, as shown in Fig. 20a. Under driving scenarios, the controller targets only humidity at the inlet while at standstill, the controller switches from humidity to CO_2 based targeting. From Fig. 20a for 0 km/h, the vapor mass fraction at the inlet follows the setpoint computed by the controller until around 25 min and then deviates, which indicates that the controller prioritizes CO_2 henceforth. This is also supported by Fig. 20b where a mean CO_2 concentration of 1000 ppm (setpoint) is achieved around the end of the simulation. A small rise in the setpoints for vapor mass fraction at the inlet is seen for with increasing driving speeds, but they remain humidity-critical for the duration of the studied scenario.

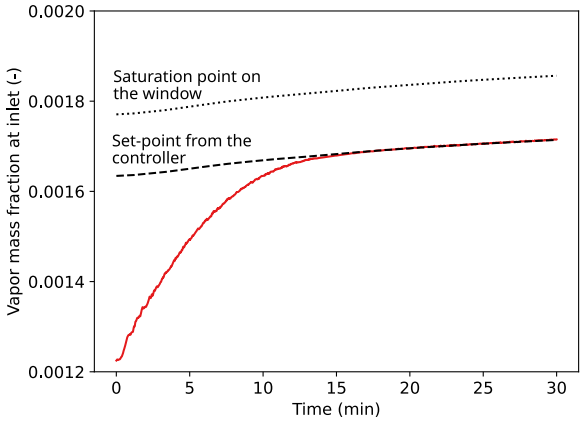

(a)

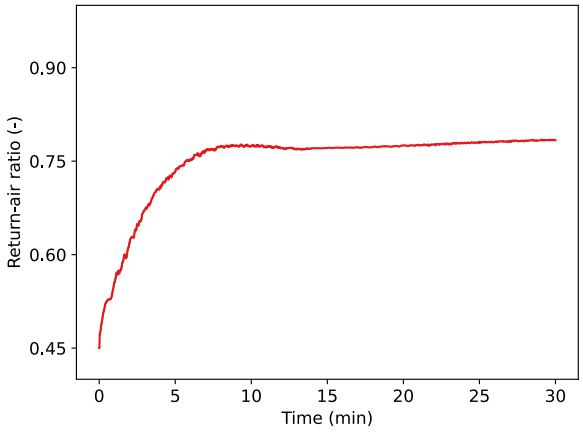

(b)

Fig. 16. Results of the RAR controller on the reference simulation: (a) Vapor mass fraction at the inlet; (b) Return-air ratio.

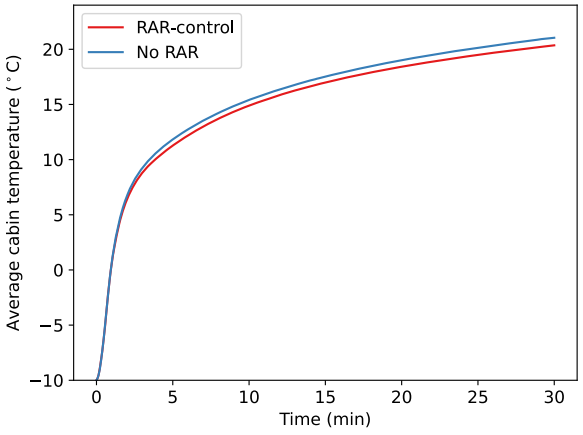

Fig. 17. Average cabin temperature comparing cases with and without RAR-control.

The resulting RAR is plotted in Fig. 20c. The mean RARs over the last minute for the various scenarios decrease with speed: 0 km/h with 87% recirculation, which is approximately the threshold for CO_2 to maintain 1000 ppm, and the 30 km/h case with 81% recirculation. The cases 60 km/h and 90 km/h have 79.3% and 78% recirculation, respectively. Thus, the driving speed influences the rate and degree to which the setpoint for inlet vapor mass fraction can be raised.

3.2.2. *Effect of varying ambient temperature*

The influence of ambient temperature was investigated while maintaining the relative humidity and vehicle speed at 70%, and 90 km/h, respectively. As seen earlier, the driving speed of 90 km/h results in high heat transfer coefficient on the external windshield and side windows.

Fig. 21 summaries the effects that ambient temperature has on RAR, the mean CO_2 concentration, and the vapor mass fraction at the inlet. The transient performance of the RAR-controller and the equalizing RAR-values to achieve the target setpoints vary with ambient temperature. The final values for the RAR were approximately 64% for -20 °C, 78% at -10 °C and 86.3% at 0 °C. The choice of these RARs corresponds to either satisfying the humidity or CO_2 criteria (1000 ppm) as seen earlier. It can be seen in Fig. 21b that at 0 °C, the mean CO_2 concentration in the cabin reaches the setpoint indicating it is more critical than humidity at this condition. However, at the other two temperatures, the CO_2 levels are lower than 1000 ppm and thus, we can infer that humidity is more critical at -20 °C and -10 °C ambient to prevent fogging. The trends for vapor mass fraction at the inlet are shown in Fig. 21c to illustrate the behavior.

Finally, the energy consumption and the energy savings, compared to the corresponding case without RAR, are presented in Fig. 22. It can be seen that the energy consumption of the cabin increases with decreasing ambient temperatures, while the percentage energy savings decrease due to lower RAR usage. This is to prevent fogging. At 0 °C, energy savings is about 34%. As mentioned, this operating state is limited by CO_2, with a steady-state RAR of about 86.3%. This will be further explored in the subsequent subsection.

3.2.3. *Effect of varying relative humidity*

For this study, the ambient relative humidity was varied while the temperature and vehicle speed were maintained at -10 °C and 90 km/h. As seen in the previous subsection, the temperature on the inner surfaces of the windows has only a marginal increase due to the high forced convection rate on the exterior surface.

Fig. 23a and 23b illustrate the RAR imposed on the model, and the vapor mass fraction at the inlet. It can be seen that an ambient relative humidity of 50% resulted in a RAR of approximately 86% at the end of the simulation. The setpoint for the inlet vapor mass fraction is achieved at around 25 min while the mean CO_2 concentration is the cabin is 970 ppm. Though not simulated here, the controller would switch to CO_2-critical condition when the RAR from the humidity controller exceeds 86.3%, which, as discussed earlier, corresponds to the recirculation ratio for the mean CO_2 concentration to be maintained at 1000 ppm. The other scenarios resulted in 78% final RAR at 70% relative humidity, and about 51% at 90% relative humidity. The scenario with 90% relative humidity achieves the setpoint for vapor mass fraction within 5 min of the simulation. The corresponding RAR increases from 30% to 51%. This behavior is characterized by the difference between the initial and increasing setpoints for the inlet vapor mass fraction due to the window heating up.

Fig. 23c illustrates the total energy consumption in the RAR-mode, and the energy savings compared to the corresponding scenario without recirculation. The energy consumption increased with increase in the relative humidity for the same temperature. This is because the RAR usage reduced from 86% to 51% with increase in relative humidity from 50% to 90%. The energy savings vary inline with the magnitude of RAR usage.

3.3. *Combined analysis*

The results from the parametric analyses considering the variation in ambient temperature and relative humidity are plotted together in Fig. 24. To extend the analysis, additional configurations at -20 °C with varying relative humidities are included.

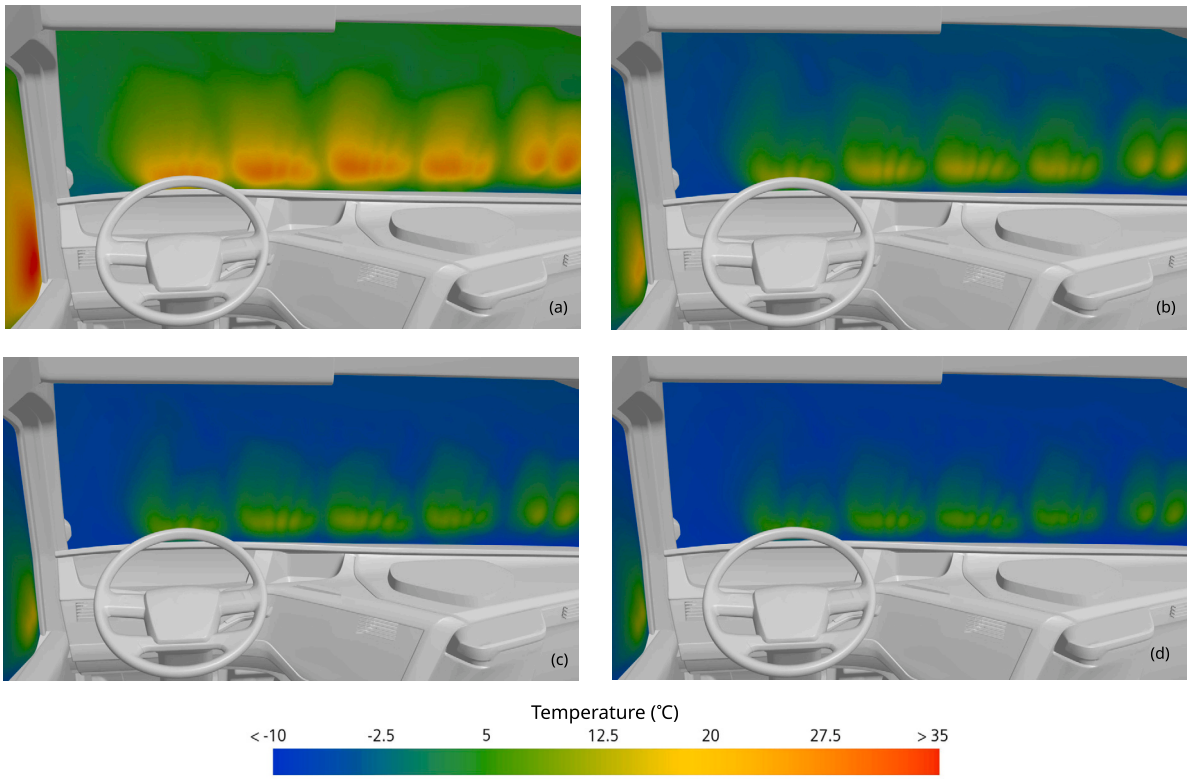

Fig. 18. Temperature on the inner windshield surface at the end of 30 minutes at -10 °C ambient temperature and 70% relative humidity: (a) v_{veh} = 0 km/h; (b) v_{veh} = 30 km/h; (c) v_{veh} = 60 km/h; (d) v_{veh} = 90 km/h.

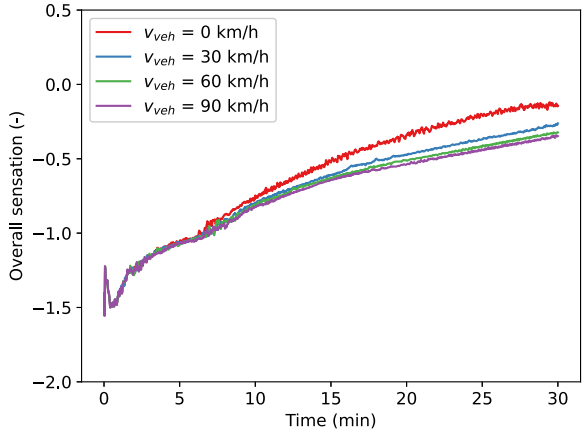

Fig. 19. Sensitivity of overall sensation of the driver with varying vehicle speeds at -10 °C and 70% relative humidity.

It can be seen that the fresh-air flow rate ($(1-\gamma)\dot{m}_{in}$) into the cabin, in Fig. 24a, decreases with Δx_ω, which represents the difference between the setpoint vapor mass fraction computed at $T_{g,min}$-1 (which varies during heat up) and the ambient vapor mass fraction, i.e. $\Delta x_\omega = x_\omega(T_{g,min} - 1) - x_{\omega,\infty}$. In the plot, each cluster of symbols represents the results from one scenario after either of the setpoints is achieved. A clear trend is observed, meaning that irrespective of the ambient temperature and relative humidity, the Δx_ω determines the amount of fresh air required. This trend should be valid at any driving speed as seen in Section 3.2.1. For each scenario, the amount of fresh air required decreases since the windows heat up, thus increasing the Δx_ω. The maximum RAR of approximately 86.3% corresponding to fresh air flow rate of 10 g/s, maintains the mean cabin CO_2 concentration at 1000 ppm as shown in previous literature [9,17]. The steady-state solution from the 0-D cabin (derived in Appendix A.4, eqn. (A.4.5)) is plotted with an uncertainty band. As seen, it is in excellent correlation with the results from CFD. The uncertainty stems from the amount of sweating from the manikin, varying from 18 to 25 g/h, depending on the clothing resistance (Table A.3.1) employed in eqn. (8) for a given scenario. This agrees well with the observations in previous studies [20,33]. While the correlation is good, the small deviations between the solutions from the two models can be attributed to the local vapor mass fraction and the CO_2 concentrations at the REC boundaries in CFD, which can not be captured in the 0-D model. Additionally, the presence of open REC outlet changes the flow behavior around the dashboard and floor as described in Section 3.1.

In Fig. 24b, the net energy savings are plotted as a function of mean RAR over the last 5 min of the scenario. They increase linearly with RAR until the threshold for CO_2 is met at 86.3% RAR. At this point, the trend deviates between different ambient temperatures. This can be explained by rearranging eqn. (16) and eqn. (17) as,

$$Q_{heater,k} = \dot{m}_{in} c_p \left[\left(T_{in,k}|_{(T_{cab},T_\infty)} - T_\infty \right) - \gamma|_{\Delta x_\omega,k} \left(T_{REC,k} - T_\infty \right) \right] \tag{25}$$

The setpoint for the inlet temperature is a function of the mean cabin and ambient temperatures. As explained from Fig. 24a, the RAR is dependent on the Δx_ω. The net energy savings relative to no recirculation can be defined from eqn. (25) as,

$$\Delta Q_{heater}\% = \frac{\sum_k \gamma|_{\Delta x_\omega,k}(T_{REC,k} - T_\infty)}{\sum_k T_{in,k}|_{(T_{cab},T_\infty)} - T_\infty} \times 100 \tag{26}$$

The expression describes the linear dependency between energy savings and RAR. This also explains the lower energy savings at lower ambient temperatures. The energy savings at 0 °C ambient temperature and 70% relative humidity is marginally higher than -10 °C and 50% RH, even though they operate at 86% RAR, due to the inherently lower energy requirement (smaller denominator in eqn. (26)) to heat up the cabin. It must be mentioned that the net energy savings for the investigated

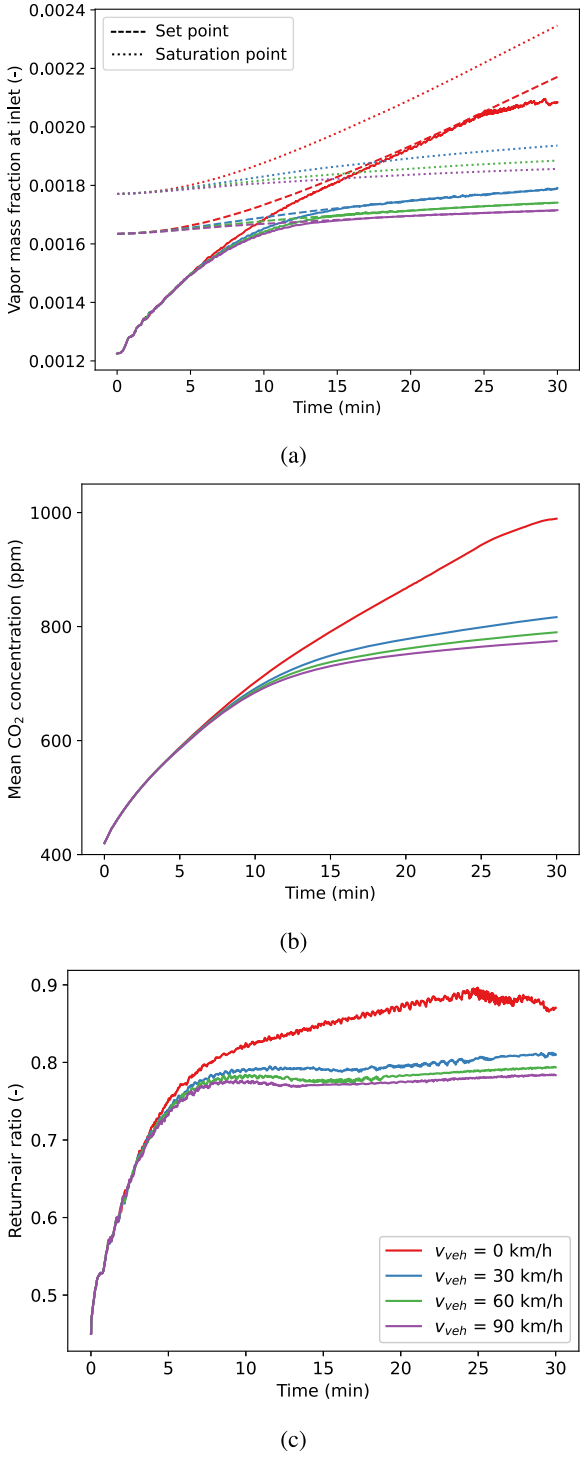

Fig. 20. Results from the sensitivity analysis with varying vehicle speed at -10 °C ambient temperature and 70% relative humidity: (a) Vapor mass fraction at the inlet; (b) Mean CO_2 in the cabin; (c) Return-air ratio.

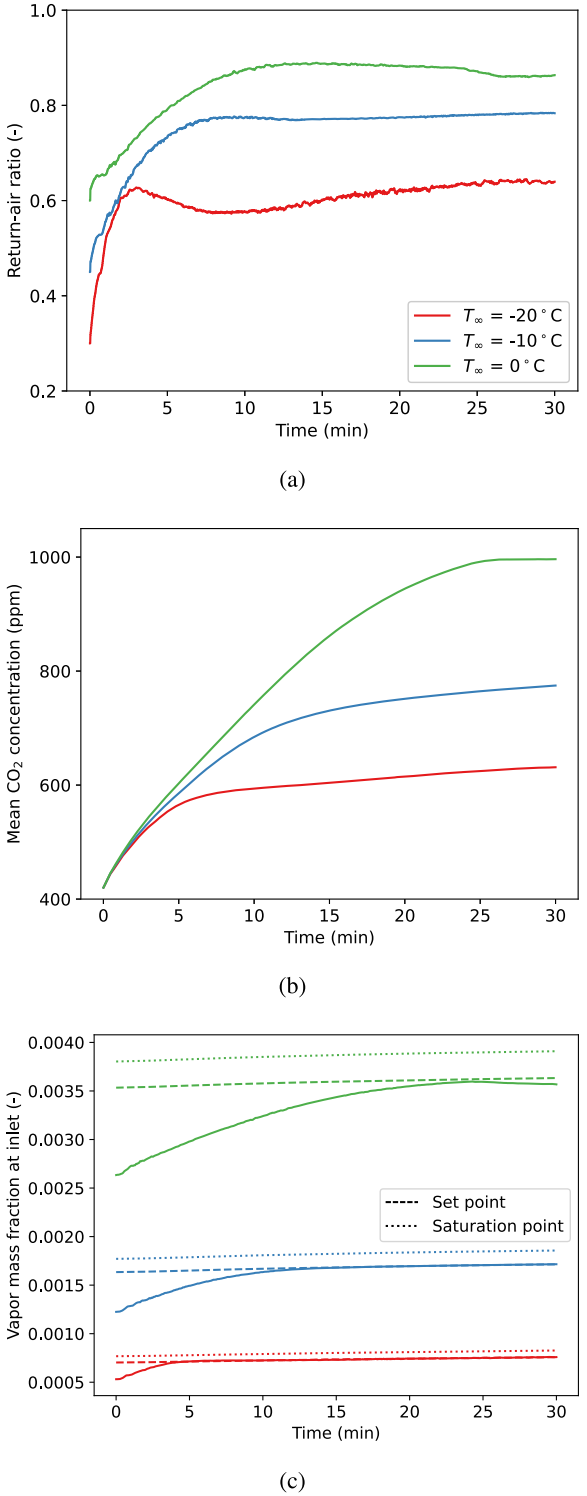

Fig. 21. Results from the sensitivity analysis with varying ambient temperature at 70% relative humidity and 90 km/h driving speed: (a) Return-air ratio; (b) Mean CO_2 concentration and (c) Vapor mass fraction at the inlet.

scenario is typically lower since T_{REC} and γ increase during the heat-up phase. The instantaneous energy saving was more than 41% for the reference case at the end of 30 min.

3.4. Effect of the number of occupants and HVAC inlet mass flow rate

The 0-D steady-state solution model (Appendix A.4) demonstrated a good correlation with CFD. To further extend the analysis, this simplified model was employed to investigate the effect of the number of occupants and the mass flow rate into the cabin on the return-air ratio, under different Δx_ω. Fig. 25a and 25b illustrate the variation of RAR with one and two occupants, respectively. The results can be summarized as:

1. The RAR increases with Δx_ω for a given inlet mass flow rate until the CO_2 setpoint is met, which is represented by the black dotted line in Fig. 25.

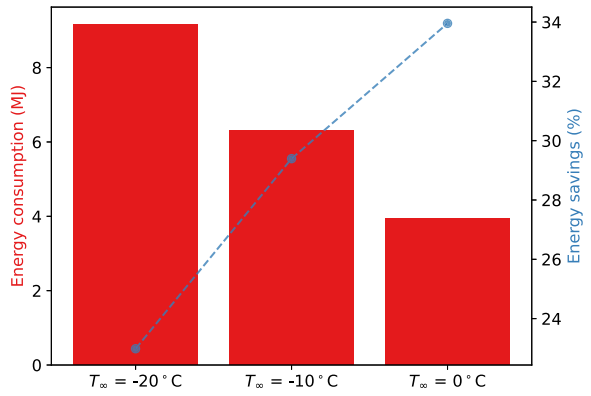

Fig. 22. Variation in the energy consumption (Y1, in red) with the ambient temperatures using RAR-control with 90 km/h driving speed and 70% relative humidity. The energy savings (Y2, in blue) relative to the corresponding scenario without recirculation.

2. For a given Δx_ω, the RAR increases with the mass flow rate into the cabin.
3. At a given Δx_ω and mass flow rate into the cabin, the RAR reduces with increasing number of occupants.

Equation (A.4.5) is independent of the volume of air in the cabin, thus, the solution is valid for any cabin size or geometry, provided there is a good correlation between the mean species concentration and that at the REC outlets in the cabin. The energy savings with RAR are linearly dependent on the RAR employed as seen in eqn. (26) and, hence, must follow the same trend. This means the energy consumption increases with the number of occupants in the cabin since RAR usage is reduced. With some calibration, the steady-state solution (eqn. (A.4.5)) or the contour plots of Fig. 25 can be implemented as look-up tables for RAR control under real-world scenarios.

4. Conclusion

The current work employed a co-simulation strategy of CFD and JOS-3 thermoregulation models to analyze the effectiveness of an adaptive RAR strategy on the heat-up performance of an electric truck. The main conclusions from the study are as follows:

- Local flow interactions and high heat loss from the manikin, especially the limbs and face, had a large influence on sensation and comfort. These segments typically have low clothing resistances, thus indicate the necessity of local heaters for improved thermal comfort.
- The use of recirculation during heating resulted in a small reduction in the mean cabin temperatures as compared to the case without recirculation, but had no effect on the overall sensation and comfort.
- The driving speed had a significant effect on the rate of heat loss from the windows, which influenced the RAR strategy greatly. The difference between the setpoint and ambient vapor mass fractions (Δx_ω) was identified to be a scenario independent parameter for appropriate RAR estimation. A decreasing trend was observed for the fresh air requirement with increasing Δx_ω up to about 10 g/s, which was required for maintaining the mean CO_2 concentration at 1000 ppm. The energy savings were also found to be linearly proportional to the RAR, as compared to the scenarios without recirculation.
- The analytical solution for recirculation had excellent correlation with the results from the co-simulation making it a viable option for real-world RAR estimation. The solution is valid for any cabin size and geometry, provided a good correlation exists between the mean species concentrations and that at the REC outlets in the cabin.
- The recirculation ratio that can be employed increases with the HVAC inlet mass flow and decreases with the number of occupants.

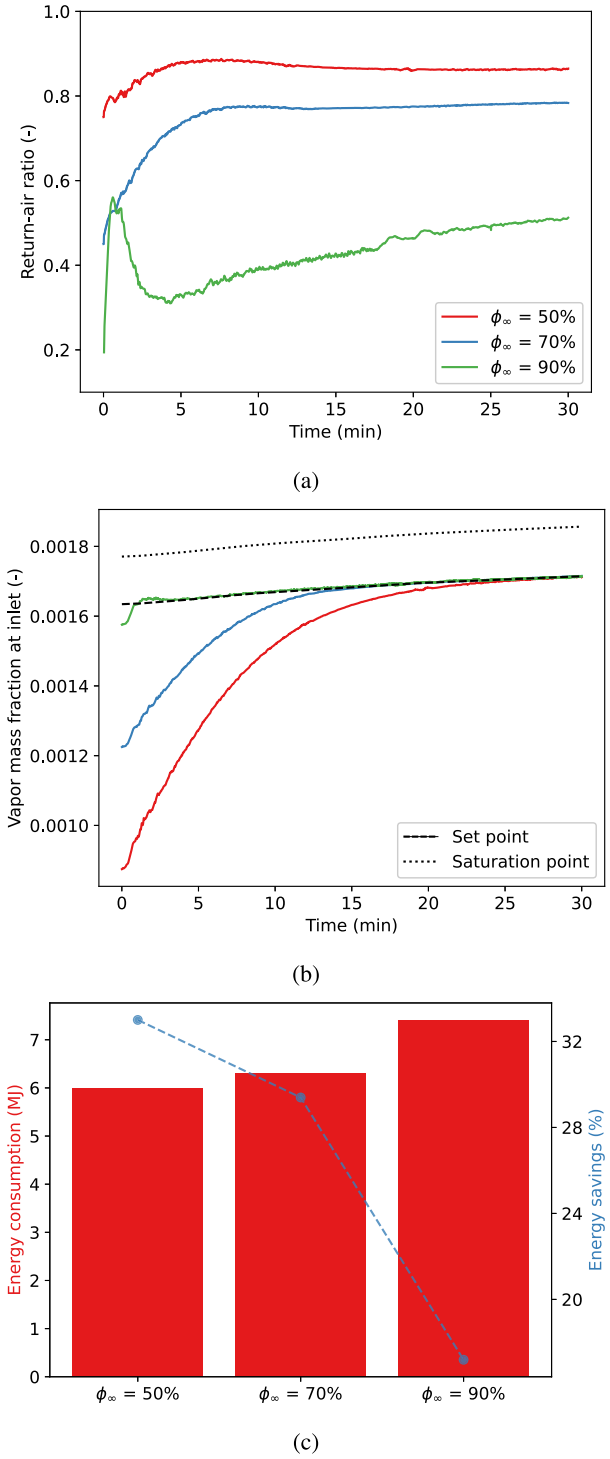

Fig. 23. Results from the sensitivity analysis with varying relative humidity at -10 °C ambient temperature and 90 km/h driving speed: (a) Return-air ratio; (b) Vapor mass fraction at the inlets and (c) Energy consumption using RAR-control (Y1, in red) and energy savings (Y2, in blue) relative to the corresponding scenario without recirculation.

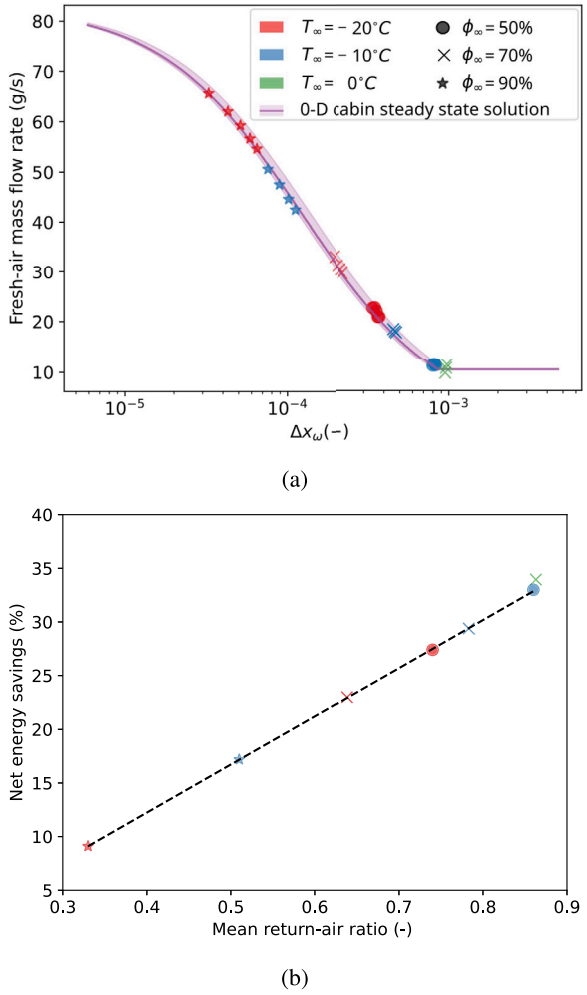

Fig. 24. Combined analysis based on the sensitivity studies of ambient temperature and relative humidity at 90 km/h: (a) Variation of fresh-air flow rate into the cabin versus the difference between setpoint and ambient vapor mass fractions at the inlet (Δx_ω); (b) Variation of net energy savings vs return-air ratio.

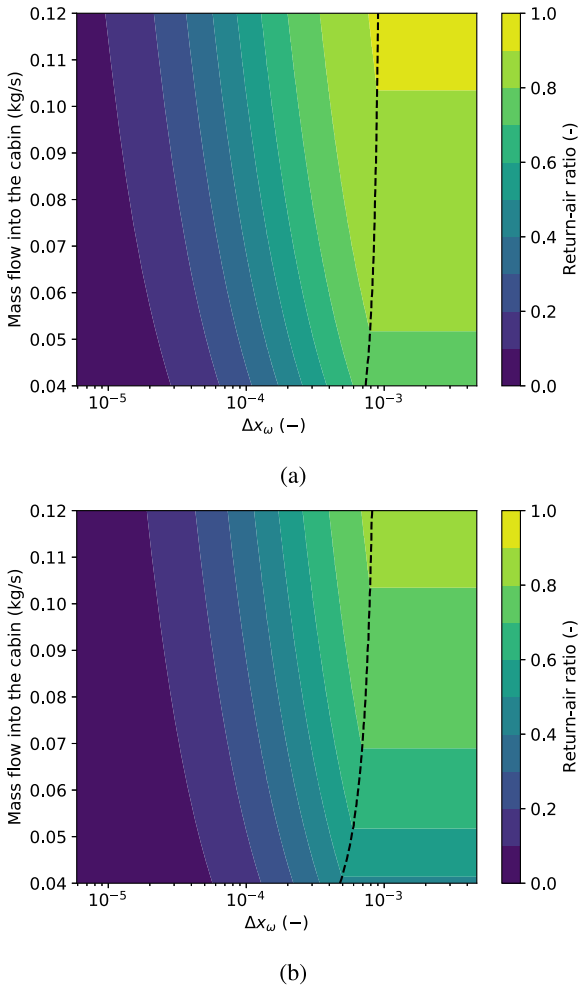

Fig. 25. The effect of mass flow rate into the cabin and the difference between the setpoint and ambient vapor mass fractions in the inlet (Δx_ω) on the return-air ratio with: (a) One occupant; (b) Two occupants. The black dotted line represents the point where the CO_2 criterion is met.

CRediT authorship contribution statement

Anandh Ramesh Babu: Writing – original draft, Visualization, Validation, Software, Methodology, Investigation, Formal analysis, Data curation, Conceptualization. **Simone Sebben:** Writing – original draft, Supervision, Resources, Project administration, Investigation, Funding acquisition, Conceptualization. **Zenitha Chronéer:** Writing – review & editing, Validation, Supervision, Software, Methodology, Investigation, Conceptualization. **Sassan Etemad:** Writing – review & editing, Supervision, Resources, Project administration, Investigation, Conceptualization.

Declaration of competing interest

The authors declare that they have no known competing financial interests or personal relationships that could have appeared to influence the work reported in this paper.

Data availability

The authors do not have permission to share data.

Acknowledgements

The authors would like to sincerely thank Dr. Fredrik Bruzelius at Chalmers University of Technology for his valuable contributions in developing the control strategy.

The computations and data handling were enabled by resources provided by the National Academic Infrastructure for Super computing in Sweden (NAISS) and the Swedish National Infrastructure for Computing (SNIC) at NSC Linköping University, partially funded by the Swedish Research Council through grant agreements no. 2022-06725 and no. 2018-05973.

Appendix A

A.1. Cabin solid material properties

The material properties of the cabin solids used in the CHT model are displayed in Table A.1.1.

A.2. External CFD simulation

The vehicle was placed in a rectangular domain of dimensions 136 m×9 m×7m, typical of aerodynamic simulations. The surfaces of the truck were set to a constant temperature (T_s) of 10 °C, and the air was blown with a temperature of 0 °C (T_∞) at various speeds (30 km/h, 60

Table A.1.1
Thermophysical properties of the solids in the vehicle cabin [7,38–40].

Solid ID	Usage	Density (kg/m^3)	Specific capacity (kJ/kgK)	Thermal conductivity (W/mK)
S1	Side windows	2500	8400	1.4
S2	Windshield	2338	754	1.1717
S3	Door panels, IP Top storage covers	908	1883	0.26
S4	Floor, motor wall	1030	1913	0.31
S5	Roof	440	1500	0.1
S6	Side, rear walls	1270	1700	0.2
S7	Bunk, seats	410	1210	0.05
S8	Ducts, bunk lower wall	1211	900	0.15
S9	Door mid-panel	908	1400	0.19
S10	Door reinforcements	7832	434	64

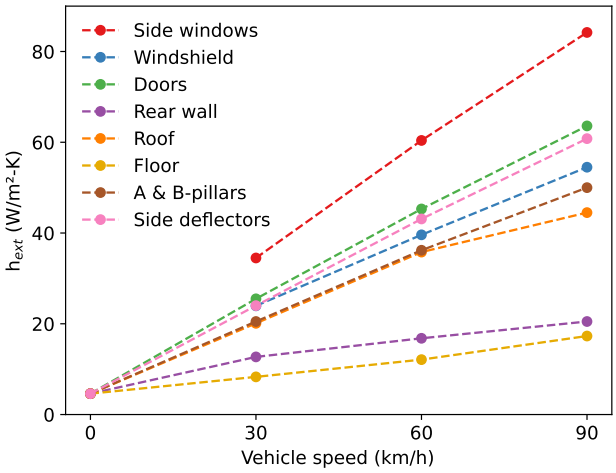

Fig. A.2.1. Variation in the heat transfer coefficient on the external vehicle surface with vehicle speed.

km/h, and 90 km/h). The SST $k-\omega$ (RANS) turbulence model was used to model air with constant density corresponding to an ambient pressure of 1 atm and 5 °C. The same air velocity was used on the ground, with a moving wall boundary condition to achieve the desired relative motion between the vehicle and the ground. The outlet was modeled as a pressure outlet boundary condition with the same temperature as the ambient.

The average heat flux (q_s'') for each surface was computed at different speeds, and the external heat transfer coefficient (h_{ext}), plotted in Fig. A.2.1 was estimated using the expression,

$$h_{ext,s} = \frac{q_s''}{T_s - T_\infty} \tag{A.2.1}$$

The heat transfer coefficient is a function of Reynold's number (Re) and Prandtl number (Pr), when process is forced convection-dominant. Hence, imposing a constant h_{ext} is valid under these conditions. However, at standstill conditions, the heat transfer coefficient is in the natural convection regime, where it is a function of the temperature difference between air and the wall temperature [24,41]. Hence, the empirical equation of Nusselt number (Nu) for natural convection of a vertical plate was employed as a field function on the outer side of the front and side windows.

$$Nu = 0.59(Gr_L.Pr)^{1/4} = \frac{h_{ext}.L}{\lambda} \tag{A.2.2}$$

where Gr is the Grashof number, and L is the length scale. A value of 4.65 W/m^{2}K was used on the other outer walls based on previous works [42–44] when the vehicle was at a standstill condition. The same value was used on the outer surfaces of the dashboard and the ducts under all vehicle speeds.

Table A.3.1
Clothing resistance on JOS-3 depending on the ambient temperature.

Ambient Temperature (°C)	Clothing Resistance (clo)				
	Head	Torso	Hand	Pants	Feet
0	0	0.9	0.1	0.9	0.1
-10	0	1.3	0.15	1.3	0.15
-20	0	1.5	0.2	1.5	0.2

A.3. Clothing resistance

The total clothing resistance on the driver was considered based on the ambient temperatures according the recommendations from Rintamaki et al. [45] for a low-moderate activity level. This was divided into five and applied to individual segments in JOS-3 as shown in the Table A.3.1.

A.4. Steady-state solution for the recirculation ratio from a 0-D cabin model

The transport of specific humidity (ω) in the lumped model with one control volume can be described as,

$$m_{cab}\frac{d\omega}{dt} = \dot{m}_{in}(\omega_{bo} - \omega) + \dot{m}_h\omega_h \tag{A.4.1}$$

where m_{cab} the mass of air in the cabin, $\dot{m}_{in}$ is the mass flow rate of air from the HVAC system, $\dot{m}_h\omega_h$ is the rate at which vapor is introduced by the human. The first term on the right-hand side represents the HVAC contribution to humidity transport and the second term represents the source term from the human.

Assuming that the specific humidity at the recirculation outlet is equal to the mean concentration in the cabin, the specific humidity from the blower (ω_{bo}) can be defined as,

$$\omega_{bo} = \gamma\omega + (1-\gamma)\omega_\infty \tag{A.4.2}$$

where ω_∞ is the ambient specific humidity. Depending on the minimum temperature of the glass, the inlet setpoint for specific humidity can be defined using eqn. (21) as $\omega(T_{g,min} - 1, 100\%)$.

At steady-state condition, the left-side term in eqn. (A.4.1) is zero. Substituing eqn. (A.4.2) into eqn. (A.4.1), the recirculation ratio at steady-state for satisfying the humidity criterion (γ_ω) can be defined as,

$$\gamma_{\omega,ss} = \frac{1}{1 + \frac{\dot{m}_h\omega_h}{\dot{m}_{in}(\omega_{in,set} - \omega_\infty)}} \tag{A.4.3}$$

The transport of CO_2 (α) in a lumped model can be described similarly to eqn. (A.4.1). Upon following the same steps, to maintain 1000 ppm mean concentration in the cabin, the steady-state recirculation ratio for CO_2 criterion can be defined as,

$$\gamma_{\alpha,ss} = 1 - \frac{\dot{m}_h \alpha_h}{\dot{m}_{in}(\alpha_{set} - \alpha_\infty)} \tag{A.4.4}$$

The final steady-state RAR is,

$$\gamma_{ss} = \min(\gamma_{\omega,ss}, \gamma_{\alpha,ss}) \tag{A.4.5}$$

A.5. Recirculation ratio PI-controller parameter

The tuning parameter c used in eqn. (23), was derived based on the steady-state estimation of simplified lumped cabin model and defined as,

$$c = \gamma_{ss} m_{cab} \frac{(\omega_{in,set} - \omega_\infty)}{\dot{m}_h \omega_h} \tag{A.5.1}$$

This formulation was realized through benchmarking to produce with low overshoot (to prevent fogging) from the setpoint under all conditions.

References

[1] European Union, Setting co2 emission performance standards for new heavy-duty vehicles and amending regulations, (ec) no 595/2009 and (eu) 2018/956 of the european parliament and of the council and council directive 96/53/ec, 2019.

[2] Filip Nielsen, Åsa Uddheim, Jan-Olof Dalenbäck, Potential energy consumption reduction of automotive climate control systems, Appl. Therm. Eng. (ISSN 1359-4311) 106 (2016) 381–389, https://doi.org/10.1016/j.applthermaleng.2016.05.137, https://www.sciencedirect.com/science/article/pii/S1359431116308158.

[3] John Taggart, Ambient temperature impacts on real-world electric vehicle efficiency & range, in: 2017 IEEE Transportation Electrification Conference and Expo (ITEC), IEEE, 2017, pp. 186–190.

[4] Norm Meyer, Ian Whittal, Martha Christenson, Aaron Loiselle-Lapointe, The impact of driving cycle and climate on electrical consumption & range of fully electric passenger vehicles, in: Proceedings of EVS, vol. 26, 2012, p. 11.

[5] Matthew A. Jeffers, Larry Chaney, John P. Rugh, Climate control load reduction strategies for electric drive vehicles in cold weather, SAE Int. J. Passeng. Cars, Mech. Syst. (ISSN 1946-4002) 9 (1) (April 2016) 75–82, https://doi.org/10.4271/2016-01-0262, https://www.sae.org/content/2016-01-0262/.

[6] Steffen Wirth, Frank Niebling, Umashankar Logasanjeevi, Vijay Premchandran, Improved thermal insulation for contemporary automotive roof structures based on a computational fluid dynamics heat flux approach, Heat Transf. Eng. 37 (16) (2016) 1418–1426, https://doi.org/10.1080/01457632.2015.1136170.

[7] Anandh Ramesh Babu, Simone Sebben, Tore Bark, Effect of cabin insulation on the heating performance in EVs at low temperatures, Detroit, Michigan, United States, pp. 2023–01–0763, https://doi.org/10.4271/2023-01-0763, https://www.sae.org/content/2023-01-0763, Apr. 2023.

[8] Guiying Zhang, Huiming Zou, Fei Qin, Qingfeng Xue, Changqing Tian, Investigation on an improved heat pump AC system with the view of return air utilization and anti-fogging for electric vehicles, Appl. Therm. Eng. (ISSN 1359-4311) 115 (March 2017) 726–735, https://doi.org/10.1016/j.applthermaleng.2016.12.143, https://www.sciencedirect.com/science/article/pii/S1359431116345070.

[9] Dixin Wei, Filip Nielsen, Hannes Karlsson, Lars Ekberg, Jan-Olof Dalenbäck, Vehicle cabin air quality: influence of air recirculation on energy use, particles, and co2, Environ. Sci. Pollut. Res. Int. (2023) 1–16.

[10] Jason A. Lustbader, John P. Rugh, Jonathan M. Winkler, Eugene V. Titov, Sourav Chowdhury, Lindsey Leitzel, Mark Zima, Mark Santacesaria, Aamir Khawaja, Murali Govindarajalu, Total thermal management of battery electric vehicles (bevs), Technical report, National Renewable Energy Lab. (NREL), Golden, CO (United States), 2018.

[11] Yoichiro Higuchi, Hiroyuki Kobayashi, Zhiwei Shan, Mikiharu Kuwahara, Yoshiharu Endo, Yuha Nakajima, Efficient heat pump system for phev/bev, Technical report, SAE Technical Paper, 2017.

[12] Sara Bellocchi, Giuseppe Leo Guizzi, Michele Manno, Marco Salvatori, Alessandro Zaccagnini, Reversible heat pump hvac system with regenerative heat exchanger for electric vehicles: analysis of its impact on driving range, Appl. Therm. Eng. (ISSN 1359-4311) 129 (2018) 290–305, https://doi.org/10.1016/j.applthermaleng.2017.10.020, https://www.sciencedirect.com/science/article/pii/S1359431117338875.

[13] Jae Hwan Ahn, Hoon Kang, Ho Seong Lee, Hae Won Jung, Changhyun Baek, Yongchan Kim, Heating performance characteristics of a dual source heat pump using air and waste heat in electric vehicles, Appl. Energy (ISSN 0306-2619) 119 (2014) 1–9, https://doi.org/10.1016/j.apenergy.2013.12.065, https://www.sciencedirect.com/science/article/pii/S0306261914000051.

[14] Tong-Bou Chang, Jer-Jia Sheu, Jhong-Wei Huang, High-efficiency hvac system with defog/dehumidification function for electric vehicles, Energies 14 (1) (2020) 46.

[15] ASHRAE ANSI. Standard 62.1-2016, Ventilation for Acceptable Indoor Air Quality, American Society of Heating, Refrigerating, and Air-Conditioning Engineers, Atlanta, 2016.

[16] Gursaran D. Mathur, Experimental investigation to determine influence of build-up of cabin carbon dioxide concentrations for occupants fatigue, in: SAE 2016 World Congress and Exhibition, SAE International, Apr. 2016.

[17] Tong-Bou Chang, Jer-Jia Sheu, Jhong-Wei Huang, Yu-Sheng Lin, Che-Cheng Chang, Development of a CFD model for simulating vehicle cabin indoor air quality, Transp. Res., Part D, Transp. Environ. (ISSN 1361-9209) 62 (July 2018) 433–440, https://doi.org/10.1016/j.trd.2018.03.018, https://linkinghub.elsevier.com/retrieve/pii/S1361920917309744.

[18] Kazushi Shikata, Yukio Uemura, Yutaka Ichitani, Goro Uchida, Yasushi Kato, Development of two layer flow hvac unit, Technical report, SAE Technical Paper, 1999.

[19] Shinichiro Hirai, Takuya Kataoka, Tatsumi Kumada, Takaaki Goto, The humidity control system applied to reduce ventilation heat loss of hvac systems, Technical report, SAE Technical Paper, 2011.

[20] Manuel Lorenz, Reduction of Heating Loads and Interior Window Fogging in Vehicles, PhD thesis, Technische Universität München, 2015.

[21] Leyan Pan, Cichong Liu, Ziqi Zhang, Tianying Wang, Junye Shi, Jiangping Chen, Energy-saving effect of utilizing recirculated air in electric vehicle air conditioning system, Int. J. Refrig. 102 (2019) 122–129.

[22] Yoshito Takahashi, Akihisa Nomoto, Shu Yoda, Ryo Hisayama, Masayuki Ogata, Yoshiichi Ozeki, Shin-ichi Tanabe, Thermoregulation model JOS-3 with new open source code, Energy Build. 231 (January 2021) 110575, https://doi.org/10.1016/j.enbuild.2020.110575, https://www.sciencedirect.com/science/article/pii/S0378778820333612.

[23] Prateek Bandi, Neeraj Paul Manelil, M.P. Maiya, Shaligram Tiwari, A. Thangamani, J.L. Tamalapakula, Influence of flow and thermal characteristics on thermal comfort inside an automobile cabin under the effect of solar radiation, Appl. Therm. Eng. (ISSN 1359-4311) 203 (February 2022) 117946, https://doi.org/10.1016/j.applthermaleng.2021.117946, https://www.sciencedirect.com/science/article/pii/S1359431121013661.

[24] Frank P. Incropera, David P. DeWitt, Theodore L. Bergman, Adrienne S. Lavine, et al., Fundamentals of Heat and Mass Transfer, vol. 6, Wiley, New York, 2013.

[25] Craig J. Hickey, Richard Raspet, William V. Slaton, Effects of thermal diffusion on sound attenuation in evaporating and condensing gas-vapor mixtures in tubes, J. Acoust. Soc. Am. (ISSN 0001-4966) 107 (3) (03.2000) 1126–1130, https://doi.org/10.1121/1.428403.

[26] Carlo Gualtieri, Athanasios Angeloudis, Fabian Bombardelli, Sanjeev Jha, Thorsten Stoesser, On the values for the turbulent Schmidt number in environmental flows, Fluids (ISSN 2311-5521) 2 (2) (2017), https://doi.org/10.3390/fluids2020017, https://www.mdpi.com/2311-5521/2/2/17.

[27] Paul Danca, Florin Bode, Ilinca Nastase, Amina Meslem, On the possibility of CFD modeling of the indoor environment in a vehicle, Energy Proc. (ISSN 1876-6102) 112 (March 2017) 656–663, https://doi.org/10.1016/j.egypro.2017.03.1133, https://linkinghub.elsevier.com/retrieve/pii/S1876610217312584.

[28] Wei Liu, Jizhou Wen, Chao-Hsin Lin, Junjie Liu, Zhengwei Long, Qingyan Chen, Evaluation of various categories of turbulence models for predicting air distribution in an airliner cabin, Build. Environ. (ISSN 0360-1323) 65 (2013) 118–131, https://doi.org/10.1016/j.buildenv.2013.03.018, https://www.sciencedirect.com/science/article/pii/S036013231300098X.

[29] Fojtlín Milos, Michal Planka, Jan Fiser, Airflow measurement of the car hvac unit using hot-wire anemometry, EPJ Web Conf. 114 (2016) 02023, https://doi.org/10.1051/epjconf/201611402023.

[30] PLM Siemens, STAR-CCM+ user guide version 2210, Siemens PLM Software Inc., Munich, Germany, 2022.

[31] Bhoopendra Choudhary, Udayraj, A coupled CFD-thermoregulation model for air ventilation clothing, Energy Build. (ISSN 0378-7788) 268 (August 2022) 112206, https://doi.org/10.1016/j.enbuild.2022.112206, https://www.sciencedirect.com/science/article/pii/S0378778822003772.

[32] B.A. Kader, Temperature and concentration profiles in fully turbulent boundary layers, Int. J. Heat Mass Transf. 24 (9) (1981) 1541–1544.

[33] Faming Wang, Clothing Evaporative Resistance: Its Measurements and Application in Prediction of Heat Strain, PhD thesis, Lund University, November 2011.

[34] Tong-Bou Chang, Jer-Jia Sheu, Jhong-Wei Huang, Vehicle air leakage ventilation and its effect on cabin indoor air quality, Proc. Inst. Mech. Eng., E J. Process Mech. Eng. 231 (6) (2017) 1226–1234.

[35] Michael L. Grady, Heejung Jung, Yong chul Kim, June Kyu Park, Bock Cheol Lee, Vehicle cabin air quality with fractional air recirculation, Technical report, SAE Technical Paper, 2013.

[36] Elias Mansour, Rotem Vishinkin, Stéphane Rihet, Walaa Saliba, Falk Fish, Patrice Sarfati, Hossam Haick, Measurement of temperature and relative humidity in exhaled breath, Sens. Actuators B, Chem. (ISSN 0925-4005) 304 (February 2020) 127371, https://doi.org/10.1016/j.snb.2019.127371, https://www.sciencedirect.com/science/article/pii/S0925400519315709.

[37] Hui Zhang, Human Thermal Sensation and Comfort in Transient and Non-Uniform Thermal Environments, PhD thesis, University of California, Berkeley, 2003.

[38] Yiyi Mao, Ji Wang, Junming Li, Experimental and numerical study of air flow and temperature variations in an electric vehicle cabin during cooling and heating, Appl. Therm. Eng. (ISSN 1359-4311) 137 (2018) 356–367, https://doi.org/10.1016/j.applthermaleng.2018.03.099, https://www.sciencedirect.com/science/article/pii/S1359431117331058.

[39] Michael Kolich, Daniel Dooge, Mark Doroudian, Efim Litovsky, Richard Ng, Jacob Kleiman, Thermophysical properties measurement of interior car materials vs.

temperature and mechanical compression, SAE Int. J. Mater. Manuf. 7 (3) (2014) 646–654, ISSN 19463979, 19463987, http://www.jstor.org/stable/26268650.

[40] Jan Pokorny, Jan Fiser, Miroslav Jicha, A parametric study of influence of material properties on car cabin environment, EPJ Web Conf. 67 (2014) 02096, https://doi.org/10.1051/epjconf/20146702096.

[41] S. Mostafa Ghiaasiaan, Convective Heat and Mass Transfer, CRC Press, 2018.

[42] Huajun Zhang, Lan Dai, Guoquan Xu, Yong Li, Wei Chen, Wen-Quan Tao, Studies of air-flow and temperature fields inside a passenger compartment for improving thermal comfort and saving energy. Part I: test/numerical model and validation, Appl. Therm. Eng. (ISSN 1359-4311) 29 (10) (July 2009) 2022–2027, https://doi.org/10.1016/j.applthermaleng.2008.10.005, https://linkinghub.elsevier.com/retrieve/pii/S1359431108004183.

[43] Yiyi Mao, Ji Wang, Junming Li, Experimental and numerical study of air flow and temperature variations in an electric vehicle cabin during cooling and heating, Appl. Therm. Eng. (ISSN 1359-4311) 137 (June 2018) 356–367, https://doi.org/10.1016/j.applthermaleng.2018.03.099, https://linkinghub.elsevier.com/retrieve/pii/S1359431117331058.

[44] Yoshitaka Hayakawa, Daisuke Sato, Noboru Yamada, Measurement of the convective heat transfer coefficient and temperature of vehicle-integrated photovoltaic modules, Energies (ISSN 1996-1073) 15 (13) (2022), https://doi.org/10.3390/en15134818, https://www.mdpi.com/1996-1073/15/13/4818.

[45] Hannu Rintamäki, Sirkka Rissanen, Heat strain in cold, Ind. Health 44 (3) (2006) 427–432, https://doi.org/10.2486/indhealth.44.427.